Relativistic Effects and GRB Polarization in Power-Law Evolution

Liang Li[1,2,3], She-Sheng Xue[1,2,3], and Zi-Gao Dai[4,5]

[1]*ICRANet, Piazza della Repubblica 10, 65122 Pescara, Italy*
[2]*INAF – Osservatorio Astronomico d'Abruzzo, Via M. Maggini snc, I-64100, Teramo, Italy*
[3]*Dip. di Fisica and ICRA, Sapienza Universita di Roma, Piazzale Aldo Moro 5, I-00185 Rome, Italy*
[4]*Department of Astronomy, University of Science and Technology of China, Hefei 230026, China*
[5]*School of Astronomy and Space Science, Nanjing University, Nanjing 210023, China*

Despite decades of polarization observations and high-significance polarized γ-ray, X-ray, optical, and radio emissions in gamma-ray bursts (GRBs) have been accumulating in dozens of cases[1–7], people has yet to find a consistent scenario for understanding the globally observed timing properties of GRB polarization to date. Here, we report that the observed properties of GRB polarization exhibit a four-segment timing evolution at the cosmological distance: (I) an initial hump early on (within the first few seconds); (II) a later on power-law decay (from $\sim 10^1$ to $\sim 10^4$ s), which takes the form of $\pi_{\rm obs} \propto t^{-0.50\pm0.02}$; (III) afterwards a late-time rebrightening hump (from $\sim 10^4$ to $\sim 10^5$ s); and (IV) finally a flatting power-law decay (from $\sim 10^5$ to $\sim 10^7$ s), with the the form of $\pi_{\rm obs} \propto t^{-0.21\pm0.08}$. These finding may present a challenge to the mainstream of polarization models that assume the polarization time evolution change in different emission regions. We show that these results can be explained by relativistic and geometric effects[8] of a highly relativistic and magnetized jet generated by central engine, and "magnetic patches"[9–12] distributed as a globally random but locally coherent form. The long-term timing evolution of observed GRB polarization follows a scaling law $\pi_{\rm obs} \propto 1/S_{\rm obs}$, dominantly determined by how "magnetic patches" are randomly distributed in observed emission region $S_{\rm obs}$ on the jet plane of $1/\Gamma$ cone. It predicts the polarization hump and tail form in accordance with the luminosity jet break phenomenon. Our analysis suggests that there is a single dominant mechanism (relativistic and geometric effects) that might account for the global observational properties of GRB polarization, and other emission mechanisms and effects might play a role in spatially local and temporally short effects on GRB polarization.

Measuring the polarization from GRB emission play a crucial role in understanding the physics of relativistic jets–in particular–providing a unique probe of the magnetic fields in the collimated jets[13–18]. After more than two decades of polarimetric observations, GRB polarimetric measurements have accumulated in dozens of cases[2,4,5], and have been observed in both early and late emission phases, spanning from a few seconds to a few months (covering six to seven orders of magnitude in time) after the burst trigger, making it possible to study GRB polarization properties in a global manner.

Despite decades of multi-wavelength observations and considerable theoretical efforts, there is still no a consistent scenario for explaining the globally observed timing properties of GRB po-

larization to date. A better understanding of the physics of GRB polarization properties is required to have a more complete picture of the long-timescale evolutionary connections from burst to burst. Therefore, we searched the literature for published and archival observations that would allow us to provide a complete picture of polarization evolution. With this dedicated search, the complete GRB polarization sample, which consists of 73 bursts (39 bursts with known redshifts) and covers a broad wavelength range (from radio to γ-ray) of polarization measurements, is provided (see Table 1).

In order to investigate the temporal properties of GRB polarization, a corresponding epoch of the polarization measurement for each burst is required. In order to explore the intrinsic properties of GRB polarization at the cosmological distance, a time-dilation correction factor 1/(1+z) is applied. The degree of polarization ($\pi_{\rm obs}$) as a function of time after the burst plotted in the cosmological rest-frame is shown in Figure 1 for the full polarization sample (with known redshift, see Table 1). By modeling the data, we discover that the globally time-sampled evolutionary properties of GRB polarization degrees $\pi_{\rm obs}$ (percentages, ranging from 0% to 100%) consist of four segments (Figure 1): (I) an initial hump early on (within the first few seconds); (II) a power-law decay over a long-term timescale period (from $\sim$$10^1$ to $\sim$$10^4$ s) later on, which takes the form of $\pi_{\rm obs} \propto t^{-0.50\pm0.02}$ with a decay index around at -0.50 (see Methods); (III) a rebrightening hump occurs at a later time (from $\sim$$10^4$ to $\sim$$10^5$ s); and (IV) finally, a new power-law decay (from $\sim$ 10^5 to $\sim$ 10^7 s), which takes the form of $\pi_{\rm obs} \propto t^{-0.21\pm0.08}$. These observational properties are naturally in agreement with theoretical previsions based on the scenario of relativistic geometric effects and outflow dynamics (Figure 2). In the standard GRB fireball "internal-external" shock model[19–24], following the collimated relativistic outflows (jets) launched from the central engine: the early and short-lived prompt γ-ray emissions generated by an internal shock, where two consecutive shells interact and collide, occur at a close distance from the progenitor; while the late and long-lasting, X-ray, optical, and radio wavelengths afterglow emissions originated from an external shock, where outflows interact with ambient medium, occur at large distances from progenitors. Within this scenario, relativistic magnetized jets are also expected to be generated by the central engines and launched along with the relativistic collimated jets, either by hyper-accreting black holes or by rapidly spinning magnetars[1–8,13–18], very likely distributed as globally random, but locally coherent magnetic fields. A local coherent magnetic domain of typical area dimension $S_{\rm patch}$ is named as a "magnetic patch"[9–12], where magnetic field $H_{\rm patch}$ orientation is in order. It emits polarized photon about $\sim \Pi_{\rm max}$ (Eq.4). The orientations of magnetic fields and photon polarization vary from one magnetic patch to another. These magnetic patches and fields randomly distribute in a outflow due to magnetized fluid dynamics.

In early emission (within the first few seconds), starting at an bulk Lorentz factor $\Gamma \gg 1$, due to relativistic beaming, only the emission inside the 1/Γ cone can be contributed to the observed flux[9], so as to the observable area $S_{\rm obs}$ is a small portion of outflow. When only one magnetic patch in outflow is seen ($S_{\rm obs} \lesssim S_{\rm patch}$), the observed polarization $\pi_{\rm obs}$ is about $\Pi_{\rm max}$, associating to magnetic patch field $H_{\rm patch}$ and orientation. Afterwards, Γ decreases due to energy dissipation, and $S_{\rm obs}$ increases. More and more magnetic patches in outflow are seen. The observed net polarization from all magnetic patches seen should be smaller than $\Pi_{\rm max}$, attributed to globally and randomly

disorder distributions of magnetic patch fields and orientation in a outflow. The more magnetic patches are seen and contribute to the observed flux, the smaller measured net polarization is, owing to an increase of randomness degree of magnetic patches distributing over the observed area $S_{\rm obs}$. Considering that the local synchrotron radiation and magnetized fluid dynamics timescales are much smaller than the period of observed polarization data collected and analyzed, we propose that outflow relativistic and geometric effects play an essential role in explaining observed polarization properties in a long-time duration. The observed polarization $\pi_{\rm obs}$ should correspond to the net polarization averaged over magnetic patches distribution and their fluid and radiation dynamics effects. As a consequence, the $\pi_{\rm obs}$ long-time evolution mainly follows a scaling law $\pi_{\rm obs} \propto 1/S_{\rm obs}$ ($S_{\rm patch} \lesssim S_{\rm obs} \lesssim S_{\rm jet}$ and from $\sim 10^1$ to $\sim 10^4$ s) until a jet-break time (from $\sim 10^4$ to $\sim 10^5$ s) is reached when $S_{\rm obs} \approx S_{\rm jet}$ (see Methods). The scaling law seems in agreement with data. At the moment of jet-break time, an Earth based observer naturally starts to see non-axial symmetric or irregular boundaries of outflows. Such an irregular or fractal geometry of outflow boundary decrease the randomness of spatial distributions of magnetic patches, and should in principle result in net polarization increases. Therefore the scenario *a priori* previews that at jet-break time the observed polarization has an increment correlating known afterglow jet break phenomena, and change its decay scaling law from $\pi_{\rm obs} \propto 1/S_{\rm obs}$ to a shallower one, since total net polarization of entire jet is seen and the observable area $S_{\rm obs} > S_{\rm jet}$ becomes irrelevant in net polarization time evolution. In four GRBs polarization data (see Table 4), we indeed find around 10^4 to 10^5 seconds bit-increments appear correlating light-curve jet breaks, and a shallower decaying law follows after 10^5 seconds, the typical epochs and temporal slopes for jet breaks that are observed for these bursts (see Methods). We also constrain shallower decaying law in polarization data after the jet-break time ($S_{\rm obs} > S_{\rm jet}$ and $\gtrsim 10^5$ seconds), see $\Gamma \gtrsim 1$ in Figure 2, the observed net polarization decaying law clearly deviates from the scaling power law $\pi_{\rm obs} \propto 1/S_{\rm obs}$ and becomes shallower one. It may remain as a constant soon after the jet-break time, then decreases slowly, due to the time variations of magnetic patch fields and sizes, as well as magnetized outflow itself after jet break.

There are two remarks in order. First, in the first few seconds (Segment I, see Figure 1) for the early polarization evolution, the observed area should be smaller than a magnetic patch area $S_{\rm obs} < S_{\rm patch}$ because of a giant Γ, and the observed polarization $\pi_{\rm obs} \sim \Pi_{\rm max}(H_{\rm patch})$ should follow the variations of magnetic patch field $H_{\rm patch}$ and electron distribution. We speculate $\pi_{\rm obs} \sim \Pi_{\rm max}$ slightly increases, reaching its maximal value when $S_{\rm obs} \approx S_{\rm patch}$, for the possible reasons that Γ decreases, $S_{\rm obs}$ increases and more electrons (involved in) emitting radiation are observed in time. Unfortunately, current observations do not contain high-resolution polarization data for this earliest period, and we have not been able to determine the polarization evolution in time. Second, in the period after the jet break $> 10^5$ sec and $S_{\rm obs} > S_{\rm jet}$ (Segment IV, see Figure 2) for the later polarization evolution, we are lack of better-established polarization data. Therefore the power-law decay index during Segment IV is poorly constrained as determined by the current sample. To gain a deeper insight into the polarization time evolution in early (Segment I) and later (Segment IV) periods, we look forward to high-sensitivity polarimetric observations from upcoming instruments[10] to establish well-sampled polarization light curves in these two periods. It will be subjects for future studies.

In addition to the time-sampled polarization lightcurve from observed data, we also discuss other observational evidences supporting the scaling law in Segment II and bit-increment in Segment III. In Segment II ($S_{\rm patch} \lesssim S_{\rm obs} < S_{\rm jet}$), the observed net polarization mainly follows a scaling law $\pi_{\rm obs} \propto S_{\rm obs}^{-1}$ and $S_{\rm jet}/S_{\rm obs} = \theta_j^2/\theta_e^2$ (see Methods). Due to relativistic beaming, only the emission inside the $1/\Gamma$ cone contributes to the observed flux, one has $\theta_e \simeq \Gamma^{-1}$. One therefore has $\pi_{\rm obs} \propto \Gamma^2$. A possible test can be made by investigating the relation between the polarization data $\pi_{\rm obs}$ and Lorentz factor $\Gamma(\pi)$ and the latter is measured in the same epoch of polarization data (see Methods). Since $\Gamma(\pi)$ cannot be precisely estimated for certain bursts, one can use Γ_0 as a proxy. An empirical relation[11,12] ($\Gamma_0 \simeq 249 L_{\gamma,{\rm iso},52}^{0.30}$) is used to estimate the values of Γ_0, as long as their energy flux F_γ and redshift are known (see Methods). Extended Data Figure 6 shows $\pi_{\rm obs}$ as functions of Γ_0. We find the data points indeed cluster around the scaling law $\pi_{\rm obs} \propto \Gamma^2$ (see the solid lines of Figure 6), where various external shock models are considered. Moreover, in the epoch of jet-break (Segment III, $S_{\rm obs} \approx S_{\rm jet}$), we find five bursts (GRB 990510, GRB 010222, GRB 020405, GRB 030328, and GRB 080928) that exhibit the bit-increment polarization data. It is further shown that in these bursts the occurrences of polarization bit-increments are in agreement with the jet-break analysis using their afterglow data, where three (or possibly four) bursts may observe a jet break (see Methods).

The intrinsic mechanisms and effects that account for GRB polarization are complicated. The observed net polarization should come from the different microscopic radiation mechanisms and macroscopic effects of jet geometries, viewing angles, magnetic field configurations, and degree of magnetized jet, etc. Our data and theoretical analysis suggest that the relativistic geometrical effect is the dominant one across various emission regions, naturally explaining the observed power-law evolution of GRB polarization in a long time scale $\mathcal{O}(10^6)$ seconds. This single power-law over long time scales across multiple emission regions challenges the current mainstream of polarization models that assume different polarization properties in distinct emission regions[13–15,17], as described by these models, the temporal evolution of GRB polarization may display a "three-stage jump" pattern (see Figure 3) from early prompt emission to later afterglow "reverse-forward" shock emission regions. These results suggest that other possible mechanisms and effects (e.g., the internal/external shock model[19], the dissipative photosphere model[16,17], the ICMART model[17]) give contributions to GRB polarization in small time scales, that result in observational data scattering up and down around the power-law evolution.

We find four dramatically different segments spanning from a few seconds to a few months, covering six to seven orders of magnitude in time. They characterize a complete picture of the global timing properties of GRB polarization for the first time. Our results show that the time evolution of GRB polarization follows the power-law decay with an index $\alpha \simeq -0.50$ until the jet-break time. It may provide an empirical estimate of $\pi_{\rm obs}$ at a given time. The estimated $\pi_{\rm obs}$ value can be used for further constraints on physical models and their relevant parameters. For instance, the scaling law $\pi_{\rm obs} \propto S_{\rm obs}^{-1} \propto \Gamma^2$ gives an insight into the traditional GRB afterglow models, which describe the environment surrounding GRBs (see Figure 7 and Methods). Our result supports the afterglow scenarios of constant energy and density stratification (wind) environment[22,24]. It may disfavor the case of a large-scale ordered magnetic field advocated from the central engine

with an on-axis observation, because an rising scaling law of GRB polarization is predicted by the case; but favor the case of a large-scale ordered magnetic field with an off-axis observation. Moreover, analogously to the Amati relation[18], the GRB polairzation power law evolution in time shows though observed GRB phenomena are individually different (e.g., total energy, lightcurve, and spectrum), they have some common features in central engine and relativistic magnetized jet evolution at large scales in time and space.

References

1. Frail, D. A., Kulkarni, S. R., Bloom, J. S. & Djorgovski, S. G. GRB980703: radio transient. *GRB Coordinates Network* **141**, 1 (1998).

2. Covino, S. *et al.* GRB 990510: linearly polarized radiation from a fireball. *Astron. Astrophys.* **348**, L1–L4 (1999). astro-ph/9906319.

3. Coburn, W. & Boggs, S. E. Polarization of the prompt γ-ray emission from the γ-ray burst of 6 December 2002. *Nature* **423**, 415–417 (2003). astro-ph/0305377.

4. Mundell, C. G. *et al.* Early Optical Polarization of a Gamma-Ray Burst Afterglow. *Science* **315**, 1822 (2007). astro-ph/0703654.

5. Steele, I. A., Mundell, C. G., Smith, R. J., Kobayashi, S. & Guidorzi, C. Ten per cent polarized optical emission from GRB090102. *Nature* **462**, 767–769 (2009). 1010.1255.

6. Zhang, S.-N. *et al.* Detailed polarization measurements of the prompt emission of five gamma-ray bursts. *Nature Astronomy* (2019). 1901.04207.

7. Chattopadhyay, T. *et al.* Prompt Emission Polarimetry of Gamma-Ray Bursts with the AstroSat CZT Imager. *Astrophys. J.* **884**, 123 (2019). 1707.06595.

8. Fan, Y.-Z., Xu, D. & Wei, D.-M. Polarization evolution accompanying the very early sharp decline of gamma-ray burst X-ray afterglows. *mnras* **387**, 92–96 (2008). 0801.1517.

9. Gruzinov, A. & Waxman, E. Gamma-ray burst afterglow: Polarization and analytic light curves. *Astrophys. J.* **511**, 852–861 (1999). astro-ph/9807111.

10. Granot, J. & Königl, A. Linear Polarization in Gamma-Ray Bursts: The Case for an Ordered Magnetic Field. *Astrophys. J. Lett.* **594**, L83–L87 (2003). astro-ph/0304286.

11. Nakar, E. & Oren, Y. Polarization and Light-Curve Variability: The "Patchy-Shell" Model. *Astrophys. J. Lett.* **602**, L97–L100 (2004). astro-ph/0310236.

12. Granot, J. & Taylor, G. B. Radio Flares and the Magnetic Field Structure in Gamma-Ray Burst Outflows. *Astrophys. J.* **625**, 263–270 (2005). astro-ph/0412309.

13. Usov, V. V. Millisecond pulsars with extremely strong magnetic fields as a cosmological source of gamma-ray bursts. *Nature* **357**, 472–474 (1992).

14. Medvedev, M. V. & Loeb, A. Generation of Magnetic Fields in the Relativistic Shock of Gamma-Ray Burst Sources. *Astrophys. J.* **526**, 697–706 (1999). astro-ph/9904363.

15. Piran, T. Magnetic Fields in Gamma-Ray Bursts: A Short Overview. In de Gouveia dal Pino, E. M., Lugones, G. & Lazarian, A. (eds.) *Magnetic Fields in the Universe: From Laboratory and Stars to Primordial Structures.*, vol. 784 of *American Institute of Physics Conference Series*, 164–174 (2005). astro-ph/0503060.

16. Metzger, B. D., Giannios, D., Thompson, T. A., Bucciantini, N. & Quataert, E. The proto-magnetar model for gamma-ray bursts. *mnras* **413**, 2031–2056 (2011). 1012.0001.

17. Zhang, B. & Yan, H. The Internal-collision-induced Magnetic Reconnection and Turbulence (ICMART) Model of Gamma-ray Bursts. *Astrophys. J.* **726**, 90 (2011). 1011.1197.

18. Pudritz, R. E., Hardcastle, M. J. & Gabuzda, D. C. Magnetic Fields in Astrophysical Jets: From Launch to Termination. *S. Science Rev.* **169**, 27–72 (2012). 1205.2073.

19. Rees, M. J. & Meszaros, P. Unsteady outflow models for cosmological gamma-ray bursts. *Astrophys. J. Lett.* **430**, L93–L96 (1994). astro-ph/9404038.

20. Mészáros, P. & Rees, M. J. Optical and Long-Wavelength Afterglow from Gamma-Ray Bursts. *Astrophys. J.* **476**, 232–237 (1997). astro-ph/9606043.

21. Sari, R., Piran, T. & Narayan, R. Spectra and Light Curves of Gamma-Ray Burst Afterglows. *Astrophys. J. Lett.* **497**, L17–L20 (1998). astro-ph/9712005.

22. Dai, Z. G. & Lu, T. Gamma-ray burst afterglows and evolution of postburst fireballs with energy injection from strongly magnetic millisecond pulsars. *Astron. Astrophys.* **333**, L87–L90 (1998). astro-ph/9810402.

23. Piran, T. Gamma-ray bursts and the fireball model. *Phys. Rep.* **314**, 575–667 (1999). astro-ph/9810256.

24. Chevalier, R. A. & Li, Z.-Y. Wind Interaction Models for Gamma-Ray Burst Afterglows: The Case for Two Types of Progenitors. *Astrophys. J.* **536**, 195–212 (2000). astro-ph/9908272.

Author contributions

LL led the data analysis, and contributed to part of the physical explanations. SSX proposed the theoretical model for explanations and previsions of the observational data in four-time segments. LL and SSX wrote the article. ZGD participated in discussions. All authors have reviewed, discussed, and commented on the present results and on the manuscript.

Acknowledgements

LL thank Yu Wang, Felix Ryde, Bing Zhang, Xue-Feng Wu, Jin-Jun Geng, Soroush Shakeri, Shuang-Nan Zhang, Remo Ruffini, and the ICRANet members for many helpful discussions on GRB physics and phenomena.

Author information

Correspondence and requests for materials should be addressed to LL (liang.li@icranet.org), SSX (xue@icra.it), and ZGD (dzg@nju.edu.cn).

Competing Interests

The authors declare that they have no competing financial interests.

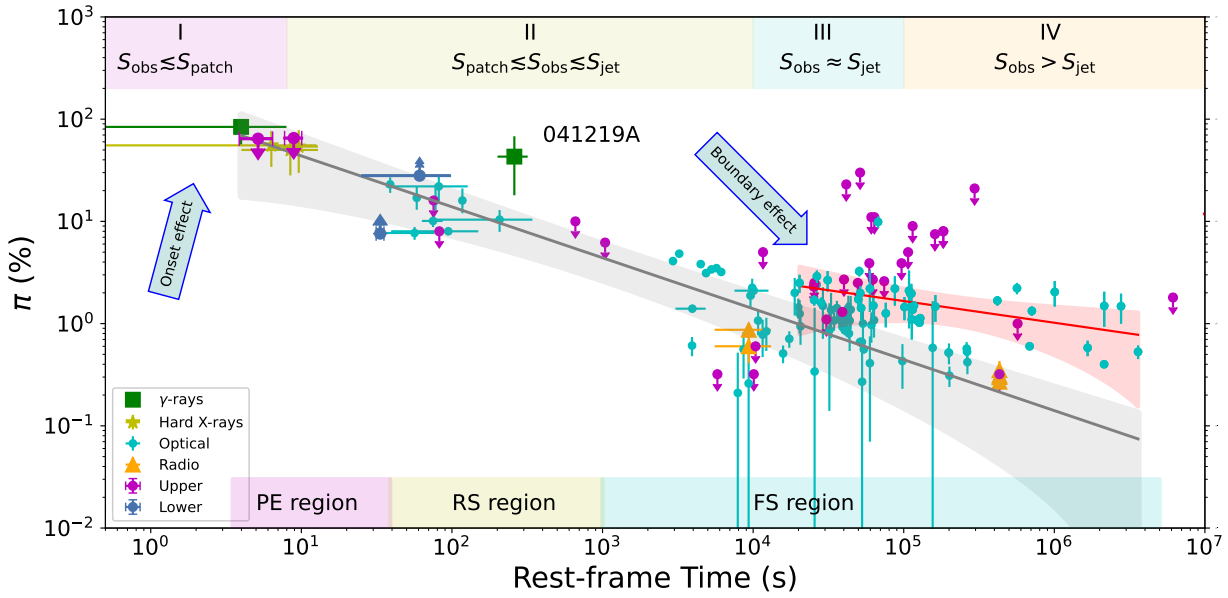

Figure 1: The degree of polarization ($\pi_{\rm obs}$, percentages ranging from 0% to 100%) for the full sample with known redshift (see Table 1) is plotted as a function of time after the burst at the cosmological distance. Data points with solid colors represent the polarization data in different energy band. Green: γ-rays; yellow: hard X-rays; cyan: optical; orange: radio; blue-magenta: the polarization data placed at the upper limits on the measurements; red-green: the polarization data placed at the lower limits on the measurements. Segment I: an initially slight hump caused by the onset effect ($S_{\rm obs} \lesssim S_{\rm patch}$) within the first few seconds. Segment II: a power-law decay ($S_{\rm patch} \lesssim S_{\rm obs} \lesssim S_{\rm jet}$) over a long timescale period (from $\sim 10^1$ to $\sim 10^4$ s), which takes the form of $\pi_{\rm obs} \propto t^{-0.50\pm0.02}$. Segment III: a late-rebrightening hump caused by the "jet break" boundary effect ($S_{\rm obs} \approx S_{\rm jet}$) occurs at a later time (from $\sim 10^4$ to $\sim 10^5$ s). Segment IV: a flatting power-law decay ($S_{\rm obs} > S_{\rm jet}$) after the "jet break" (from $\sim 10^5$ to $\sim 10^7$ s), which takes the form of $\pi_{\rm obs} \propto t^{-0.21\pm0.08}$. The solid line is the best fits using the power-law model and with 2σ (95% confidence interval) error shadow region.

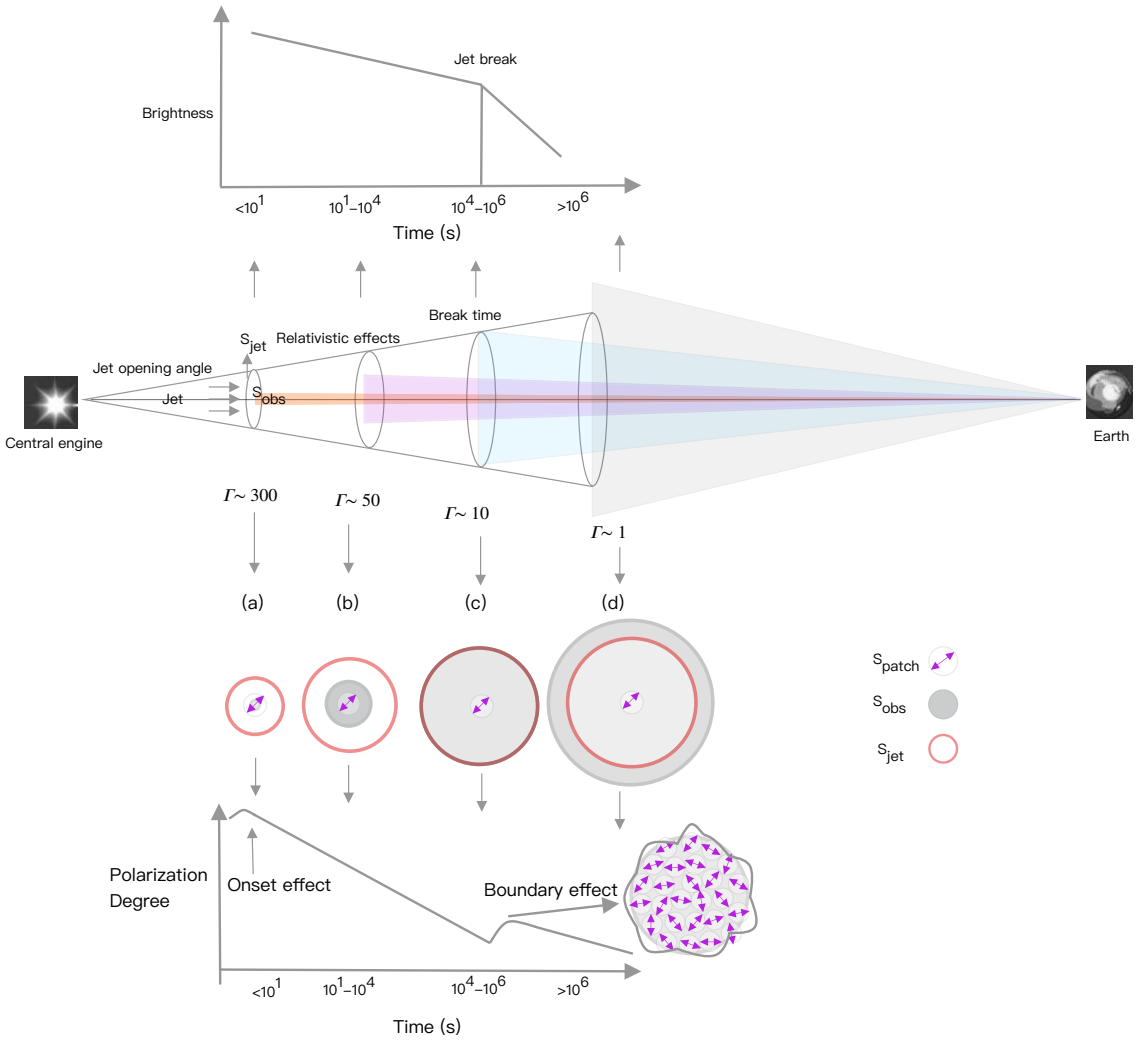

Figure 2: A cartoon picture for depicting the timing evolution of the GRB polarization degree based on relativistic geometrical effects. For simplicity, we assume that the jet opening angle θ_j remains unchanged throughout jet evolution, corresponding to an area projected onto the jet plane as $S_{\rm jet}$ (see white circle symbol in the right panel). Due to relativistic beaming, only the emission inside the $1/\Gamma$ cone contributes to the observed flux, corresponding to an observed area projected onto the jet plane as $S_{\rm obs}$ (see grey circle symbol in the right panel). A "magnetic patch" corresponds to an area projected onto the jet plane as $S_{\rm patch}$ (see orange circle symbol in the right panel). (a) The onset effect (Segment I) occurs at an early emission (within the first few seconds), corresponding to $S_{\rm obs} \lesssim S_{\rm patch}$ with a huge $\Gamma \gg 1$ (e.g., Γ=300). (b) The main power-law decay phase (Segment II) occur over a long timescale period (from $\sim 10^1$ to $\sim 10^4$ s), corresponding to $S_{\rm patch} \lesssim S_{\rm obs} \lesssim S_{\rm jet}$ with a moderate Γ (e.g., Γ=50). (c) The "jet break" boundary effect (Segment III) occurs at a later emission when the "jet break" is reached (from $\sim 10^4$ to $\sim 10^5$ s), corresponding to $S_{\rm obs} \approx S_{\rm jet}$ with a relatively low Γ (e.g., Γ=10). (d) Finally the new power-law decay phase (Segment IV) occurs after the "jet break" (from $\sim 10^5$ to $\sim 10^7$ s), corresponding to $S_{\rm obs} > S_{\rm jet}$ with a small Γ (e.g., Γ=1).

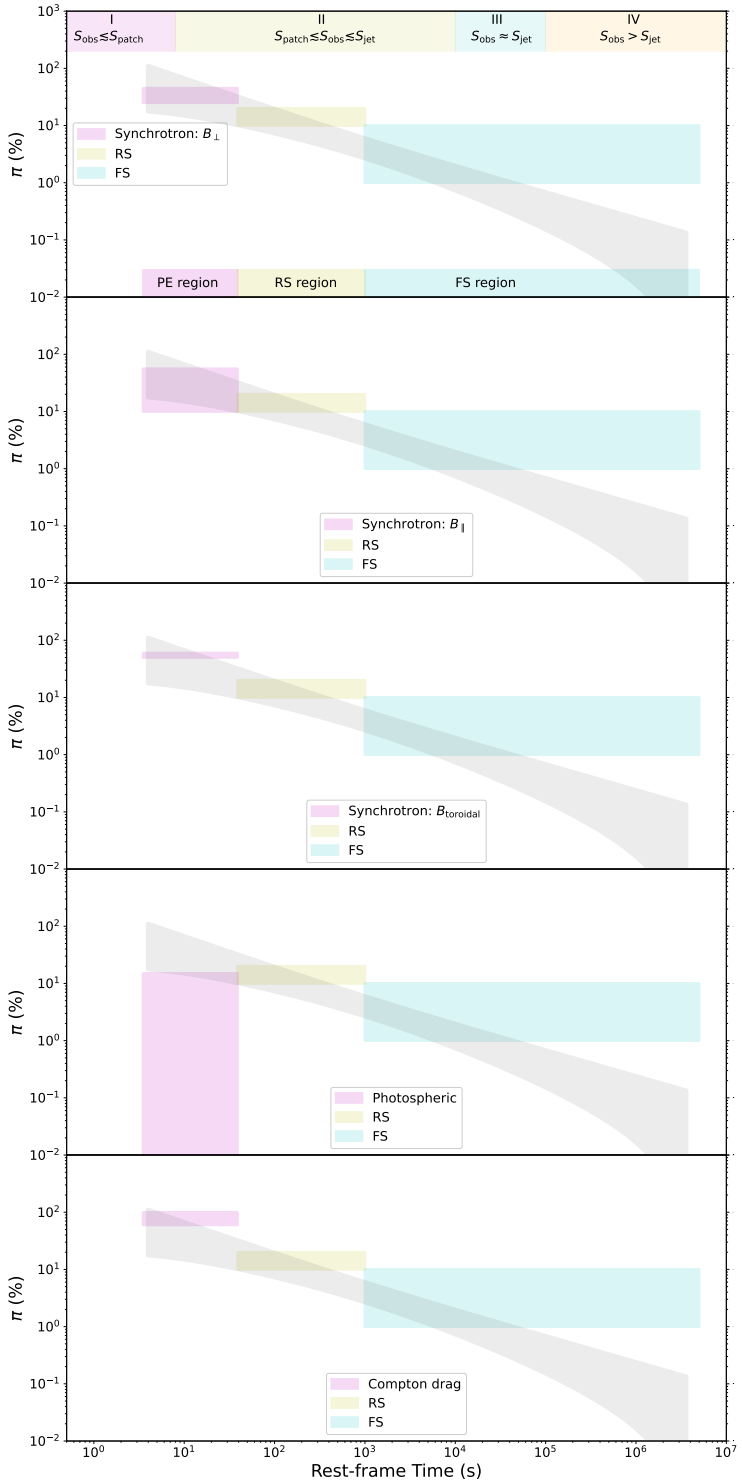

Figure 3: The contrast between the observed polarization degree and the theoretical predictions by different radiation mechanisms[19]. In the prompt emission (PE) phase, we consider the synchrotron radiation from different magnetic field structures: (a) a random field normal to the radial direction $B_\perp$ ($\pi \sim 25\%$-45%); (b) an ordered field radial $B_\parallel$ ($\pi \sim 10\%$-56%); (c) a toroidal $B_{\rm tor}$ ($\pi \sim 50\%$-60%), as well as (d) photosphere emission model ($\pi \sim 0\%$-15%); (e) Compton drag model[20] ($\pi \sim 60\%$-100%). In the afterglow emission phase, we consider the highly polarized reverse-shock (RS,[21,22]) emission ($\pi \sim 10\%$-20%), and forward-shock (FS,[9]) emission ($\pi \sim 1\%$-10%).

Methods

The GRB polarimetric sample We conducted an extensive search of the literature for published and archival polarimetric observations, and attempted to include all the bursts that had polarization measurements to date. With this dedicated search, the complete GRB polarization sample, which consists of 73 bursts (39 bursts with known redshifts, see Figure 1) and covers a broad wavelength range (from radio to γ-ray emission) of polarization measurements, is provided (see Table 1).

These observed polarization data are categorized into three types of data sets: i) Time-integrated polarization data, which represent average polarimetric properties, for the entire emission period are treated as a single time event, resembling the approach used in GRB spectral analyses; ii) Time-resolved polarization data, in which the whole emission period is divided into multiple timing events, and polarimetric measurements, are therefore performed on each event individually; iii) Polarimetric measurements are placed on an upper/lower limit. We note that (1) For a given burst, time-integrated polarization data can in principle include as many numbers of detected photons as possible, thereby reducing the uncertainties and avoiding unreliable fluctuations introduced by the time-resolved data; (2) The polarization data for a good fraction of the bursts have placed an upper/lower limit on the measurements, and therefore, this data set may not be as tightly constrained (has a loose constraint) to the model as on the other data sets.

Modeling the multi-wavelength time-sampled polarization data In order to explore the timing properties of GRB polarization, a corresponding epoch of the polarization measurement for each burst is required. To investigate the intrinsic properties of GRB polarization, we select those bursts whose redshift measurements are also reported. Extended Data Figure 1 shows that the time-integrated polarization degree $\pi_{\rm obs}$ (percentage, ranges from 0% to 100%) as a function of its corresponding epoch in the cosmological rest-frame, plotting in logarithmic-logarithmic space. As an initial result, we discovered that $\pi_{\rm obs}$ tends to be smaller over time. Figure 1 shows the polarization degree $\pi_{\rm obs}$ as a function of time $t/(1+z)$ after the burst at the cosmological distance for the full sample, where t =($T_{\rm stop}$+$T_{\rm start}$)/2), and $T_{\rm start}$ and $T_{\rm stop}$ are the start time and stop time of the related epoch listed in the Table 1, and errors $\sigma_{\rm t}$ can be calculated by $\sigma_{\rm t}$=($T_{\rm stop}$-$T_{\rm start}$)/2, and z is reshift. Using this full sample, we find that the polarization lightcurve can be best fitted by the power-law model ($\pi = At^{-\alpha}$), the best-fit function gives

$$\log_{10}(\pi_{\rm obs})/(\%) = (4.40 \pm 0.36) + (-0.498 \pm 0.020) \times \log_{10}[t/(1+{\rm z})]/({\rm s}), \quad (1)$$

with the number of data points N=115, the Spearman's rank correlation coefficient of R=-0.86, and a chance probability $p < 10^{-9}$. These results indicate that the time-sampled polarization evolution over long-timescale periods decays as a power-law[1] at cosmological distances, which takes the form of $\pi_{\rm obs} \propto [t/(1+z)]^{-0.50\pm0.02}$.

[1]It's worth noting that the "t_0" effect might have a significant impact on how early polarization evolves. This happens often in multi-pulse bursts in which adjacent pulses are well-separated by a long quiescent period. The zero time on polarization measurements may need to be corrected to be physical due to the GRB trigger time being no longer special in such cases.

Correlation coefficient analysis from the Markov chain Monte Carlo algorithm Our analysis results were also double-checked using a correlation coefficient analysis from the Markov chain Monte Carlo algorithm. The correlation coefficient can be used to assess the reliability of the correlation between the cosmological rest-frame time $t/(1+z)$ and the GRB observational polarization (π) for our samples. By implementing the Python package PyMC3, ref.[23], we use a normal-LKJ correlation prior distribution and the Markov chain Monte Carlo (MCMC) algorithm to obtain the covariance matrix of the multivariate normal distribution, and the correlation coefficient between the parameters is obtained as a result[24] by iterating 10^5 times and burning the first 10^4 times of the MCMC samples. Our results are summarized in Table 1, including the expected values (μ_1) and standard deviation (σ_1) of the normal distribution of the analyzed parameters, and their correlation coefficients, as well as the related Highest Density Interval (HDI) of the posterior distributions, ranging from 3% to 97%. In Extended Data Figure 4, we show an MCMC iteration for the mean values and standard deviation of the t_z and π, and their correlation coefficient, including the value of 10^5 iterations (right) and their distribution (left).

Results of correlation coefficient of Markov chain Monte Carlo algorithm

Sample	μ_1 (t_z)	σ_1 (t_z)	μ_2 (π)	σ_2 (π)	Correlation Coefficient [3% to 97%]	hdi interval
Time-integrated GRB polarization data	2.112±0.253	0.941±0.049	1.044±0.145	0.537±0.042	-0.950±0.028	[-0.985 to -0.902]

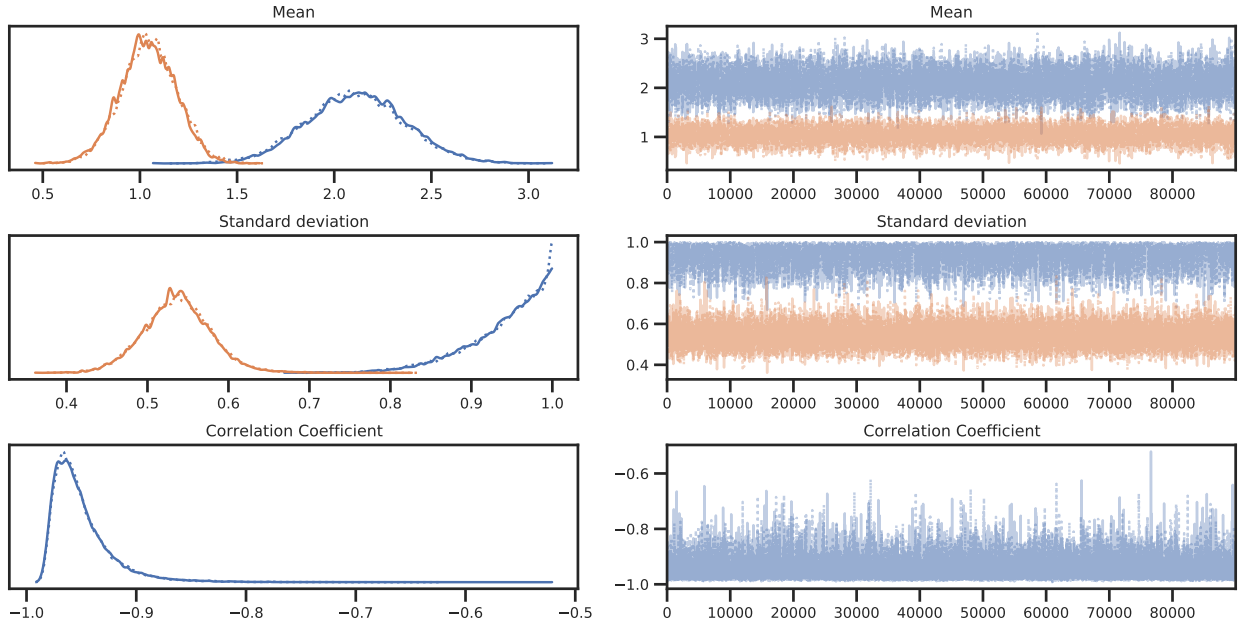

Figure 4: MCMC iteration for the mean values and standard deviation of the t_z and π, and their correlation coefficient for our sample, including the value of 10^5 iterations (right) and their distribution (left).

"Magnetic patch" polarization properties and the $\Pi_{\rm max}$ point After a relativistic jet is emitted, the outflow is likely to carry a fraction of the magnetic field energy in the form of a random magnetic field, known as relativistic magnetized jets. In this random magnetic field, the degree of order of the magnetic field is related to the observed area. The smaller the area is, the higher the

degree of order it contains. Naturally, there is a critical area, $S_{\rm patch}$, know as "magnetic patch[9–12]", where the magnetic field can be considered to be completely ordered. As shown a yellow arrowed spot in sketch Figure 2, we indicate the "magnetic patch", where magnetic field orientations are in order, producing polarized photons[2]. The magnetic patch area is $S_{\rm patch}$ and its contribution to the observed polarization is about $\Pi_{\rm max}$, where $\Pi_{\rm max}$ is the possibly maximal polarization.

In astrophysical observations, the photon polarization is measured by using the percentages (ranging from 0% to 100% percent) of polarized and non-polarized photons to represent the degree of GRB polarization, namely the measured polarization degree is given by

$$P_{\rm obs} = \pi_{\rm obs} = \frac{I^{\rm p}}{I^{\rm p} + I^{\rm n}}, \tag{2}$$

where $I^{\rm n}$ and $I^{\rm p}$ respectively refer to the intensities of the natural and fully polarized lights from the source. There are two components: fully polarized photons (e.g., elliptical, circular, and linear polarized light) and non-polarization photons (natural light). The former is completely polarized with $\pi = 1$, and the latter is completely non-polarized with $\pi = 0$. We illustrate in Figure 1 the observed $\pi_{\rm obs}$ data and their uncertainties.

The measured $\pi_{\rm obs}$ receives all contributions from the area $S_{\rm obs}$ on the jet plane visible to the observer. As discussed soon, the initial $S_{\rm obs}$ is smaller than a magnetic patch area $S_{\rm patch}$. First we introduce the polarization degree of photons emitted from a "magnetic patch", correspondingly to the observation one (Eq.2),

$$\pi_{\rm patch} = \frac{I^{\rm p}_{\rm patch}}{I_{\rm patch}}, \tag{3}$$

where $I_{\rm patch} = I^{\rm p}_{\rm patch} + I^{\rm n}_{\rm patch}$, and $I^{\rm p}_{\rm patch}$ and $I^{\rm n}_{\rm patch}$ correspond to the intensities of natural and fully polarized lights from a "magnetic patch". It can be seen from Figure 1 that the time-integrated polarization lightcurve at $S_{\rm obs} \approx S_{\rm patch}$ is a peak, from which we define as $\Pi_{\rm max}$,

$$\Pi_{\rm max} = \pi_{\rm obs} \mid_{S_{\rm patch} \approx S_{\rm obs}} \approx \pi_{\rm patch}. \tag{4}$$

Based on observations (within the uncertainties), the value of $\Pi_{\rm max}$ could be estimated to be between 70 and 100 percent (see Figure 1). Given a GRB source and its surrounding, we assume that magnetic patches have the similar structure of locally coherent domain, thus the $\Pi_{\rm max}$ of different patches are considered to be approximately the same. The reasons are given below.

When the observed area $S_{\rm obs}$ becomes larger than many magnetic patches, the observed polarization degree $\pi_{\rm obs}$ contributed by photons coming from different magnetic patches. Moreover, all magnetic patches are randomly distributed in entire observed area $S_{\rm obs}$. The net polarization degree $\pi_{\rm obs}$ is expected to be smaller than $\Pi_{\rm max}$ and monochromatically decrease in time, as the number of observed magnetic patches increases[9–12]. Thus the $\Pi_{\rm max}$ (Eq.4) represents a maximal polarization degree in observation. While the net polarization degree $P_{\rm obs}$ contributed by polarised photons from all visible patches will be defined in due course.

[2]Here, instead of specifying how the magnetic domain is form, we refer such patch to the region where polarized photons are produced in general.

Magnetic field orderliness and relativistic geometrical effects in GRB polarization We follow the discussions in jet-break phenomenon, the observed area $S_{\rm obs}$ (see grey circular area in Figure 2) varies in time depending on the bulk Lorentz factor Γ of the outflow. The evolution of such relativistic effects on observed polarization may consist of four possible segments depending on whether the observed area ($S_{\rm obs}$) is greater (or less) than the magnetic patch area ($S_{\rm patch}$) and the area ($S_{\rm jet}$) at the break time.

When the Lorentz factor $\Gamma \gg 1$ (early emission phase, such as when the outflow becomes optically transparent), due to a huge Γ, the observed cone ($\sim 1/\Gamma$) is very small. Only one or a few magnetic patches are seen, depending on magnetic patch size. If only one magnetic patch is seen, the observed area $S_{\rm obs}$ is smaller than and increasing to the magnetic patch area $S_{\rm patch}$ (Segment I, see $\Gamma \sim 300$ in Figure 2), we therefore obtain $\pi_{\rm obs} \approx \Pi_{\rm max}$ for $S_{\rm obs} \lesssim S_{\rm patch}$ from (Eqs.5-8). Indeed, as shown by three data points in the Segment I, the observed photon polarization $\pi_{\rm obs}$ very slightly increases and reach its maximal value. However, detail analysis and data need to consider also the time evolution of random magnetic fields in their sizes and strengths for slightly increasing $\Pi_{\rm max}$ value in the Segment I. This is a subject of future study. Nevertheless, using the data at initial time (around 0-10 s), we can infer the maximal value of polarization degree $\Pi_{\rm max} S_{\rm patch}/S_{\rm obs}$ for $S_{\rm patch} \approx S_{\rm obs}$ in $\Gamma \sim 300$ in Figure 2.

When the the observed area $S_{\rm obs}$ is larger than $S_{\rm patch}$ (Segment II, see $\Gamma \sim 50$ in Figure 2), it covers more than one magnetic patch. The orientations of magnetic fields and photon polarizations vary from one patch to another, see right illustration in Figure 2. Suppose that the magnetic patch $S_{\rm patch}$ emits the polarized radiation of total intensity $I_{\rm patch}$ and polarized intensity $\mathbf{I}^{\rm p}_{\rm patch}$. Here the bold $\mathbf{I}^{\rm p}_{\rm patch}$ represents the orientated polarization intensity of the value $I^{\rm p}_{\rm patch} = |\mathbf{I}^{\rm p}_{\rm patch}|$. The intensities $I_{\rm patch}$ and $I^{\rm p}_{\rm patch}$ are assumed to be approximately equal for all magnetic patches. The observed area $S_{\rm obs} \approx \sum_{S_{\rm patch}} S_{\rm patch}$ is smaller than entire emission region. An Earth based observer see the total intensity and net polarization intensity of radiation emitted from all magnetic patches within the observed area $S_{\rm obs}$. Their values can be approximately expressed as

$$I^{\rm p} = \sum_{S_{\rm patch} \in S_{\rm obs}} \mathbf{I}^{\rm p}_{\rm patch} S_{\rm patch} \approx I^{\rm p}_{\rm patch} S^{\rm eff}_{\rm patch}, \tag{5}$$

$$I \approx \sum_{S_{\rm patch} \in S_{\rm obs}} I_{\rm patch} S_{\rm patch} \approx I_{\rm patch} S_{\rm obs}. \tag{6}$$

Here we introduce an effective patch area $S^{\rm eff}_{\rm patch}$ to represent the net polarization observed from different patches.

$$S^{\rm eff}_{\rm patch} = \sum_{S_{\rm patch} \in S_{\rm obs}} (-)^p S_{\rm patch} < S_{\rm obs}, \tag{7}$$

where the notation $(-)^p$ symbolically indicates the randomness of polarization orientations from patches, indicating the destructive (rather than constructive) phenomenon of superposition of light polarizations from different patches. Due to the relativistic beaming effect, the observed area

$S_{\rm obs} \propto \Gamma^{-2}$. The observational polarization degree $\pi_{\rm obs}$ (Eq.2) is given by

$$\pi_{\rm obs} = \frac{I^{\rm p}}{I} \approx \Pi_{\rm max}(\frac{S^{\rm eff}_{\rm patch}}{S_{\rm obs}}) \propto \Gamma^2, \tag{8}$$

where $\Pi_{\rm max} = I^{\rm p}_{\rm patch}/I_{\rm patch}$ is the patch maximal polarization degree (Eq.4). We will discuss that in long time scale when $S_{\rm obs} \gg S_{\rm patch}$, the factor $\Pi_{\rm max}S^{\rm eff}_{\rm patch}$ slowly varies compared with $S_{\rm obs}$ variation, leading to $\pi_{\rm obs} \propto S^{-1}_{\rm obs} \propto \Gamma^2$. It is one of the basic formulae of our theoretical model to study the observed polarization degree of GRBs.

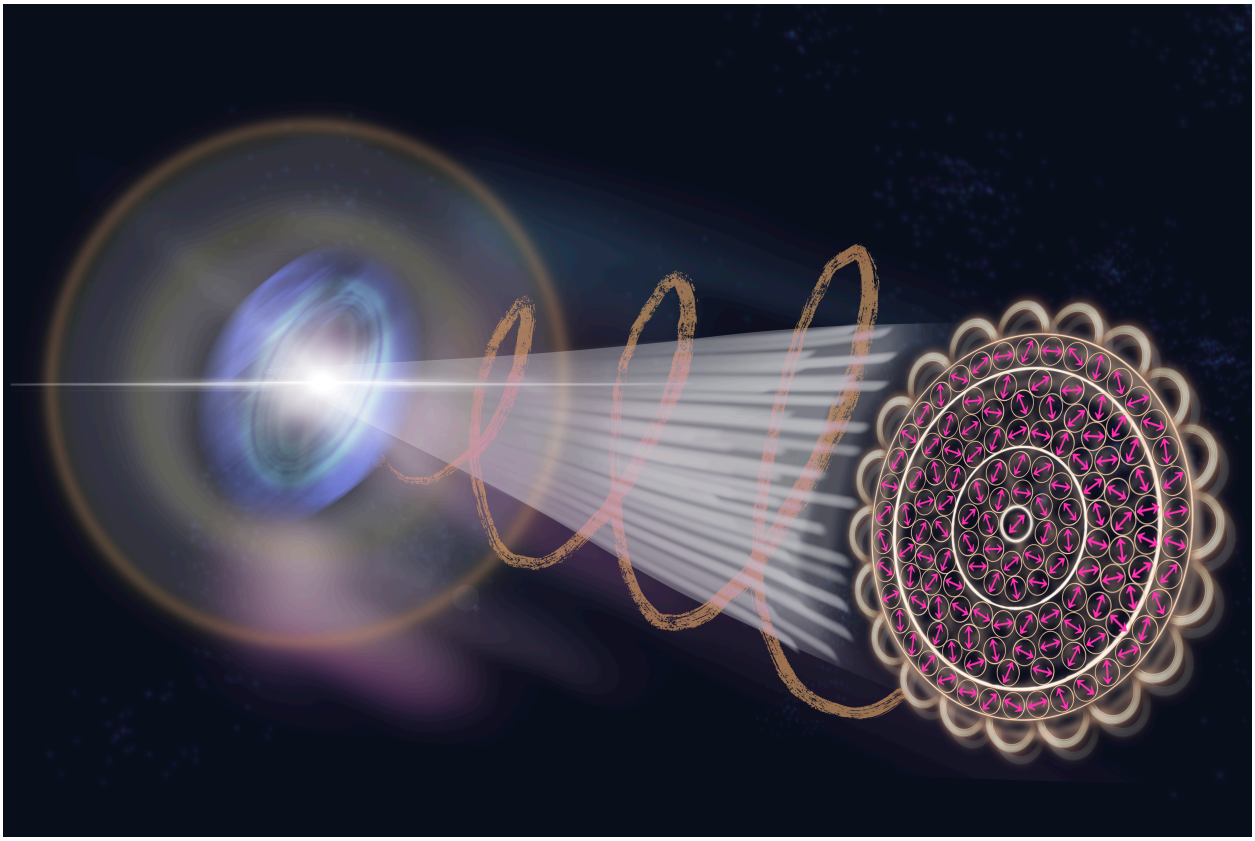

Figure 5: A cartoon picture for "magnetic patches" on the jet plane represented by many small circles with random red arrows; the observed area $S_{\rm obs} \propto 1/\Gamma^2$ increase in time represented by four hollow circles corresponding to the hollow circles in Fig.2; the irregular jet boundary represented by a waved circle.

Let us consider a GRB jet model[25,26] to illustrate the formula (Eq.8) and its time evolution. According to the jet geometry, at the distance $R_{\rm GRB} \approx ct_{\rm GRB}$ from the center engine and a fixed opening angle θ_j, the jet plane area $S_{\rm jet} \approx \hat{\pi}(\theta_j R_{\rm GRB}/2)^2$ increasing with time. The magnetic patch area on the jet plane is $S_{\rm patch} \approx \hat{\pi}(\theta_{\rm patch}R_{\rm GRB}/2)^2$. We assume that (i) the areas of magnetic patches are approximately equal and (ii) following the dynamics of jet evolution, the magnetic patches are at anchor in the jet flow. Namely, the patch opening angle $\theta_{\rm patch}$ is fixed and the total

patch number on the jet plane is approximately constant in time,

$$N_{\rm patch} \equiv \frac{S_{\rm jet}}{S_{\rm patch}} = \frac{\theta_j^2}{\theta_{\rm patch}^2} \cong {\rm const.} \quad \theta_j > \theta_{\rm patch}, \tag{9}$$

as well as the patch distribution on the jet plane are assumed to weakly depend on the jet evolution. The observed polarization $\pi_{\rm obs} \approx \Pi_{\rm max}$ is maximal, when $S_{\rm obs} \approx S_{\rm patch}$. When $S_{\rm obs} > S_{\rm patch}$, due to the fact that polarization orientations are randomly different among magnetic patches, the net polarization observed is smaller than $\Pi_{\rm max}$. Suppose that the observer is along the line-of-sight of the jet axis, i.e., approximately axial symmetric, and patch magnetic field orientations randomly distribute in the observed area $S_{\rm obs}$ (see Fig. 2 and Fig. 5). The polarizations of radiation from all magnetic patches within the observed area $S_{\rm obs}$ should almost, but not *exactly*, cancel each others. The reason is that the number of observed magnetic patches is finite and their orientations cannot be *completely* random. To represent the observer relevant net polarization of radiation from different magnetic patches, we introduce an effective patch area $S_{\rm patch}^{\rm eff}$ (Eq.7). Its value depend on the magnetic patch numbers and their random distribution inside $S_{\rm obs}$. In general, the larger $S_{\rm obs}$ is, the more $S_{\rm patch}$ are seen, the higher degree of their random distribution is, the smaller observed net polarization should be. Therefore, as increasing $S_{\rm obs}$, more and more magnetic patches are observed, the randomness of their magnetic field orientations increases, the effective patch area $S_{\rm patch}^{\rm eff}$ decreases. As a result, the net observed polarization of photons from different magnetic patches decreases. However, as $S_{\rm obs}$ becomes much larger than $S_{\rm patch}$, the polarization contributions from the patches $S_{\rm patch}$ distributing in the $S_{\rm obs}$ outer area tend to be destructive each other, due to the axial symmetry of their random distribution, as illustrated in sketch Figure 5. Namely the observed net polarization contributions mainly come from the patches $S_{\rm patch}$ distributing in the $S_{\rm obs}$ inner area. We formally express the $S_{\rm patch}^{\rm eff}$ (Eq.7) as

$$S_{\rm patch}^{\rm eff} \approx \sum_{\rm inner} (-)^p S_{\rm patch} + \sum_{\rm outer} (-)^p S_{\rm patch} \Rightarrow \sum_{\rm inner} (-)^p S_{\rm patch}. \tag{10}$$

Its approximate constancy in later time is due to the patch distribution on the jet plane is weakly time dependent, the aforementioned properties of magnetic patches on the jet plane. The discussed time evolution of $S_{\rm patch}^{\rm eff}$ is qualitatively sketched in Fig. 5.

These assumptions are on the basis that the $S_{\rm patch}$ time-varying scale $\tau_{\rm patch} \approx S_{\rm patch}^{1/2}/c$ should be smaller than $S_{\rm obs}^{1/2}/c$. In addition, the maximal polarization $\Pi_{\rm max}$ time-varying scale is smaller than $\tau_{\rm patch}$. Therefore, due to the local patch magnetic field dynamics and orientation randomness, we expect in the net polarization the factor $\Pi_{\rm max} S_{\rm patch}^{\rm eff}$ has short-time $\tau_{\rm patch}$ fluctuating features and its mean value weakly depends on time at a much long time scale ($\sim 10^5$ seconds). Thus we parametrize $\Pi_{\rm max} S_{\rm patch}^{\rm eff} \propto t^{-\alpha}$ ($\alpha \ll 1$), which varies much slowly than $S_{\rm obs}$ in time. As a result, in a long time period of data collection and analysis (Figure 1), the time dependence of observed net polarization should be dominantly determined by the time dependence of the observed area $S_{\rm obs}$, whose evolution in time is determined by relativistic effect and kinetic motion of emitting area. All above discussions can be generalized to the case that the observer line sign is not exactly along the axial symmetry line of emitting region.

The observed area $S_{\rm obs}$ on the jet plan area $S_{\rm jet}$ evolves in time. In the period of $S_{\rm patch} \lesssim S_{\rm obs} \lesssim S_{\rm jet}$ before the jet-break time scale ($\sim 10^5$ seconds), the observed net polarization mainly follow scaling law $\pi_{\rm obs} \propto 1/S_{\rm obs}$ (Eq.8) that explains in the numerical data by the following Section (see Methods). We should point out that the local and short-time fluctuating features of the factor $\Pi_{\rm max}S^{\rm eff}_{\rm patch}$ lead to the observed polarization data from GRB sources scattering around the scaling law $\pi_{\rm obs} \propto 1/S_{\rm obs}$, see Figure 2. Note that our attention is to explain such a scaling law behavior observed in jet evolution over a long time scale ($\sim 10^5$ seconds). Therefore, we ignore magnetic field and patch fluctuation in small region and short-time scales caused by local and fast varying dynamics, whose averages in a long time and large spatial scales vanish. Moreover, in observed photon polarization samples, these detail features should be also washed away by the randomness of GRB sources in their engines, surroundings and evolution histories. Only GRB common features attributed to the relativistic effect and jet geometry remain, resulting in photon polarization data scattering around the power law in time scale of 10^5 sec, see Fig. 1.

When the jet-break $S_{\rm obs} \approx S_{\rm jet}$ is reached (Segment III, see $\Gamma \sim 10$ in Figure 2), we can obtain the value $\pi_{\rm obs} \approx \Pi_{\rm max}S^{\rm eff}_{\rm patch}/S_{\rm jet}$ from data. At this moment, the non-axially symmetric jet boundary is seen, and $S^{\rm eff}_{\rm patch}$ shows a small hump in Fig.5. Such an irregular jet boundary should in principle results in net polarization increases. This explains a slight increasing data in sketch plot in Figure 2.

After the jet-break $S_{\rm obs} > S_{\rm jet}$ (Segment IV, see $\Gamma \gtrsim 1$ in Figure 2), the observed net polarization is $\Pi_{\rm max}S^{\rm eff}_{\rm patch}/S_{\rm jet} \propto t^{-\alpha}$, which clearly deviates from the power law. It should remain as an approximate constant soon after jet break, due to the total net polarization of entire jet is observed. Later on, it is expected to slowly decrease in time, namely $\pi_{\rm obs} \propto t^{-\alpha}$, due to the slowly time variations of maximal polarization $\Pi_{\rm max}$, magnetic patch $S_{\rm patch}$ area and distribution, as well as jet dynamics. These features are illustrated by sketches in Figure 2. We show in Figure 1 $\pi_{\rm obs} \propto t^{-0.21\pm0.08}$. We note that the index $\alpha \approx 0.21$ is likely to be an upper bound due to only having only one data point after 10^5 seconds of data being used, and need to pending the availability of a sufficiently comprehensive data set. More data analysis at this point are needed, yielding a more definite result. Nevertheless, the index $\alpha \approx 0.30$ being smaller than 0.5 shows that the presented scenario for understanding polarization data is self consistent and contained. In fact, four GRBs (GRB990510, GRB010222, GRB030328, and GRB080928) exhibit the correlation between flux decaying and polarization rising at the same jet break time, which provide evidences for the present theoretical scenario.

Correlation between GRB polarization and bulk Lorentz factor Consider a conical jet with line-of-sight aligned with the jet axis and with a jet opening angle θ_j, launched from the GRB central engine (see A in Extended Data Figure 2). For simplicity, we assume that the jet opening angle θ_j remains unchanged during the epoch when the jet break happens, corresponding to an area projected onto the plane as $S_{\rm jet}$ (see white circle symbol in the right panel of Figure 2), with a radius of $R_{\rm jet}$. Due to relativistic beaming, only the emission inside the 1/Γ cone contributes to the observed flux. It projects onto the jet plane an observed area $S_{\rm obs}$ of radius $R_{\rm obs}$ (see orange circle symbol in the right panel of Figure 2).

A sketch plot is shown in Extended Data Figure 2, where A is the GRB central engine, B is the observer, O is the center point of the plane, C is the highest latitude photon on the conical jet that the relativistic emission can be observed by the observer, and D is the boundary of the conical jet on the plane. We set

$$\begin{cases} \angle \mathrm{OAC} = \alpha, \\ \angle \mathrm{OBC} = \beta, \\ \angle \mathrm{BCF} = \theta_{\mathrm{e}}, \\ \angle \mathrm{BCE} = \varphi = \frac{\theta_{\mathrm{e}}}{2}, \\ \angle \mathrm{OAD} = \tau = \frac{\theta_{\mathrm{j}}}{2}, \\ \mathrm{OC} = R_{\mathrm{obs}}, \\ \mathrm{OD} = R_{\mathrm{jet}}, \\ \mathrm{OA} = R_{\mathrm{GRB}}, \\ \mathrm{OB} = L_{\mathrm{dis}}, \end{cases} \tag{11}$$

where R_{GRB} and L_{dis} are the GRB emission radius and luminosity distance, respectively.

Due to relativistic beaming, only the emission inside the $1/\Gamma$ cone can be attributed to the observed flux. For instance, the relativistic emission produced by the photon C can be observed only inside the cone $\angle$ BCF (θ_e). One therefore has

$$\theta_e \simeq \frac{1}{\Gamma}. \tag{12}$$

Through geometric correlations, one has

$$\begin{cases} \alpha = \frac{R_{\mathrm{obs}}}{R_{\mathrm{GRB}}}, \\ \beta = \frac{R_{\mathrm{obs}}}{L_{\mathrm{dis}}}. \end{cases} \tag{13}$$

On the other hand, due to $L_{\mathrm{dis}} \gg R_{\mathrm{GRB}}$,

$$\alpha \gg \beta, \tag{14}$$

therefore,

$$\varphi = \alpha + \beta \simeq \alpha, \tag{15}$$

and

$$\theta_e = 2\varphi = 2\alpha \tag{16}$$

$$\begin{cases} R_{\mathrm{jet}} = \tau \times R_{\mathrm{GRB}} \approx \tau \times (ct_{\mathrm{GRB}}), \\ R_{\mathrm{obs}} = \alpha \times R_{\mathrm{GRB}} \approx \alpha \times (ct_{\mathrm{GRB}}) \end{cases} \tag{17}$$

where t_{GRB} is the relativistic ejecta emission time measured in the cosmological rest frame, relating to the observed time t_{obs} by $t_{\mathrm{GRB}} \simeq 2\Gamma^2 t_{\mathrm{obs}}$, ref.[27].

As shown in the sketch plot in Figure 2, the three characteristic areas are expressed as

$$\begin{cases} S_{\rm jet} = \hat{\pi}(R_{\rm jet})^2 = \hat{\pi}(\tau \times R_{\rm GRB})^2 = \hat{\pi}(\frac{\theta_j}{2} R_{\rm GRB})^2 = \hat{\pi}\frac{\theta_j^2}{4} c^2 t_{\rm GRB}^2 = \hat{\pi}(\theta_j c\Gamma^2 t_{\rm obs})^2, \\ S_{\rm obs} = \hat{\pi}(R_{\rm obs})^2 = \hat{\pi}(\alpha \times R_{\rm GRB})^2 = \hat{\pi}(\frac{\theta_e}{2} R_{\rm GRB})^2 = \hat{\pi}(\frac{R_{\rm GRB}}{2\Gamma})^2 = \hat{\pi}\frac{c^2}{4\Gamma^2} t_{\rm GRB}^2 = \hat{\pi}(c\Gamma t_{\rm obs})^2, \\ S_{\rm patch} = \hat{\pi}(\frac{\theta_{\rm patch}}{2} R_{\rm GRB})^2 = \hat{\pi}\frac{\theta_{\rm patch}^2}{4} c^2 t_{\rm GRB}^2 = \hat{\pi}(\theta_{\rm patch} c\Gamma^2 t_{\rm obs})^2. \end{cases} \tag{18}$$

In addition to the constant ratio $N_{\rm patch} \equiv S_{\rm jet}/S_{\rm patch}$ (Eq.9), we examine below the ratios that are relevant for our description of timing properties of GRB polarization,

$$N_{\rm p} \equiv \frac{S_{\rm obs}}{S_{\rm patch}} \approx (\theta_{\rm patch}\Gamma)^{-2}, \tag{19}$$

$$N_{\rm obs} \equiv \frac{S_{\rm jet}}{S_{\rm obs}} = \frac{\theta_j^2}{\theta_e^2} \approx (\theta_j\Gamma)^2, \tag{20}$$

where $N_{\rm p}$ is the number of patches on the observed area $S_{\rm obs}$ and $N_{\rm obs}$ represents a fraction of $S_{\rm obs}$ over $S_{\rm jet}$. Both $N_{\rm p}$ and $N_{\rm obs}$ are Γ and time dependent. In terms of the ratio $N_{\rm p}$, the observed polarization degree $\pi_{\rm obs}$ (Eq.8) can be rewritten as

$$\pi_{\rm obs} = \Pi_{\rm max}(\frac{S_{\rm patch}^{\rm eff}/S_{\rm patch}}{S_{\rm obs}/S_{\rm patch}}) = \Pi_{\rm max}(\frac{S_{\rm patch}^{\rm eff}/S_{\rm patch}}{N_{\rm p}}). \tag{21}$$

In the initial phase of the Segment II, when $S_{\rm obs} > S_{\rm patch}$ and $S_{\rm obs}$ covers the centre part of the jet plane, the contribution $S_{\rm patch}^{\rm eff}/S_{\rm patch} \propto \sqrt{N_{\rm p}}$ following to the probability of random distribution. Thus, the polarization degree $\pi_{\rm obs} \propto 1/\sqrt{N_{\rm p}}$, in consistent with the study of Ref.[9]. Then from Eq. (19), we obtain its Γ-dependence,

$$\pi_{\rm obs} \propto \frac{1}{\sqrt{N_{\rm p}}} \propto \Gamma, \tag{22}$$

for large polarization degree in the initial and short period. In the later phase of the Segment II, when $S_{\rm obs} \gg S_{\rm patch}$ and $N_{\rm p}$ increases, the total contribution comes from the inner and outer parts, see (Eq.10). The outer part contributions cancel among themselves due to an axial symmetry. The inner part contribution remains approximately equal due to the structure and dynamics of the jet and magnetic patch (Eq.9). As a result, the $N_{\rm p}$- and Γ-dependence of the polarization degree $\pi_{\rm obs}$ becomes

$$\pi_{\rm obs} \propto \frac{1}{N_{\rm p}} \propto \Gamma^2, \tag{23}$$

for small polarization degree in the later and long period. The Γ-dependence of (Eq.22) and (Eq.23) is distinctly different. Using observed data we examine them in Extended Data Figure 6. It indeed shows that the large polarization degree follows (Eq.22) (see yellow line in Figure 6) and the small polarization follows (Eq.23) (see cyan line in Figure 6). This supports our theoretical scenario of the time evolution of polarization degree $\pi_{\rm obs}$, described in the previous Section. This is also in accordance with our explanations that the weakly Γ-depending in the initial Segment I and in the final Segment IV, as well as $\pi_{\rm obs}$ has an increment in the Segment III at the jet break time.

Numerical results (or Self-consistency checking results) Using a typical jet opening angle θ_j=0.1, we show the ratios (numbers) $N_{\rm patch}$, $N_{\rm p}$ and $N_{\rm obs}$ as functions of time and Lorentz factor Γ in Figs. 3 and 4 respectively. The observed polarization lightcurve shows a hump at initial times 0–10 s (see Segment I in Figure 1). The peak time occurs at the point $\pi_{\rm obs} \approx \Pi_{\rm max}$ when $S_{\rm obs} \approx S_{\rm patch}$. On the other hand, we have $S_{\rm obs} \approx S_{\rm jet}$ at the jet break time $t_{\rm obs} \simeq 3\times 10^4$ seconds (see Segment III in Figure 1). At the peak time and jet break time, we numerically calculate the following quantities for consistency checks.

At the initial time $t_{\rm obs} \simeq 3$ seconds and $\Gamma \simeq 300$ for a hump $\pi_{\rm obs} \approx \Pi_{\rm max}$, $S_{\rm obs} \approx S_{\rm patch}$, we obtain

- $R_{\rm GRB} \simeq ct_{\rm GRB} = c(2\Gamma^2 t_{\rm obs}) \simeq (3\times 10^{10}{\rm cm/sec})\times 2\times (300)^2\times 3{\rm sec} = 1.62\times 10^{16}$ cm.
- $S_{\rm obs} \approx S_{\rm patch} = \hat{\pi}(c\Gamma t_{\rm obs})^2 \simeq 3.14\times (3\times 10^{10}{\rm cm/sec})^2\times (300)^2\times (3{\rm sec})^2 = 2.5\times 10^{26}{\rm cm}^2$.
- $S_{\rm jet} = \hat{\pi}(\theta_j c\Gamma^2 t_{\rm obs})^2 \simeq 3.14\times 0.1^2\times (3\times 10^{10}{\rm cm/sec})^2\times (300)^4\times (3{\rm sec})^2 = 2.25\times 10^{28}{\rm cm}^2$.
- $N_{\rm p} \equiv S_{\rm obs}/S_{\rm patch} \approx 1$.
- $N_{\rm obs} \equiv S_{\rm jet}/S_{\rm obs} \approx \theta_j^2\Gamma^2 = (0.1)^2\times (300)^2 = 900$.
- $N_{\rm patch} \equiv S_{\rm jet}/S_{\rm patch} \approx S_{\rm jet}/S_{\rm obs} = 900$.

At the jet break time $t_{\rm obs} \simeq 3\times 10^4$ seconds and $\Gamma \simeq 10$, we obtain

- $R_{\rm GRB} \simeq ct_{\rm GRB} = c(2\Gamma^2 t_{\rm obs}) \simeq (3\times 10^{10}{\rm cm/sec})\times 2\times (10)^2\times 3\times 10^4{\rm sec}) = 1.8\times 10^{17}$ cm.
- $S_{\rm obs} \approx S_{\rm jet} = \hat{\pi}(c\Gamma t_{\rm obs})^2 \simeq 3.14\times (3\times 10^{10}{\rm cm/sec})^2\times (10)^2\times (3\times 10^4{\rm sec})^2 = 2.54\times 10^{32}{\rm cm}^2$.
- $S_{\rm jet} = \hat{\pi}(\theta_j c\Gamma^2 t_{\rm obs})^2 \simeq 3.14\times (0.1)^2\times (3\times 10^{10}{\rm cm/sec})^2\times (10)^4\times (3\times 10^4{\rm sec})^2 = 2.54\times 10^{32}{\rm cm}^2$.
- $N_{\rm p} \equiv S_{\rm obs}/S_{\rm patch} \approx 900$.
- $N_{\rm obs} \equiv S_{\rm jet}/S_{\rm obs} \approx \theta_j^2\Gamma^2 = (0.1)^2\times (10)^2 = 1$.
- $N_{\rm patch} \equiv S_{\rm jet}/S_{\rm patch} \approx \frac{\theta_j^2}{\theta_{\rm patch}^2} = 900$.
- $\theta_{\rm patch} = 0.1/30$.

The results are summarized in Table 3.

Testing the $\pi_{\rm obs}$-Γ and $\pi_{\rm obs}$-[t/(1+z)] relations with observational data (Segment II) In the major power-law phase (Segment II, $S_{\rm patch} \lesssim S_{\rm obs} \lesssim S_{\rm jet}$), we have obtained two important scaling laws: the observed net polarization mainly follows a scaling law $\pi_{\rm obs} \propto S_{\rm obs}^{-1} \propto \Gamma^2$ (Eq.8), and $S_{\rm jet}/S_{\rm obs} = \theta_j^2/\theta_e^2 \propto \Gamma^2$ (Eq.20), due to relativistic beaming effect. In Figure 6, we show that the scaling law $\pi_{\rm obs} \propto \Gamma^2$ is consistent with GRB data.

There are several external-shock models widely discussed in the literature. The simplest model invokes a decelerating blastwave that enters the self-similar regime with constant energy (adiabatic and no energy injection), and constant medium density (ISM)[20,21]. Several other more complicated cases, such as the dynamics of a blastwave with a varying ambient medium density (e.g., stellar wind[22,28]), or varying total energy in a blastwave (e.g., with radiative loss[27] or with energy injection[29]) have also been discussed. These traditional external-shock models give

$$\begin{cases} \Gamma \propto R_{\rm GRB}^{-3/2} \propto t^{-3/8}, R_{\rm GRB} \propto t^{1/4}; & \text{ISM} \\ \Gamma \propto R_{\rm GRB}^{-1/2} \propto t^{-1/4}, R_{\rm GRB} \propto t^{1/2}; & \text{wind}, \\ \Gamma \propto R_{\rm GRB}^{-3} \propto t^{-3/7}, R_{\rm GRB} \propto t^{1/7}; & \text{Radiative fireball}, \\ \Gamma \propto R_{\rm GRB}^{-\frac{5}{6}} \propto t^{-\frac{5}{16}}, R_{\rm GRB} \propto t^{\frac{3}{8}}; & \text{Energy injection} \end{cases} \tag{24}$$

Note that the energy injection case has taken a typical value of q=0.5.

Relativistic effects gives

$$S_{\rm obs} \propto \theta_e^2 \propto \Gamma^{-2} \tag{25}$$

The geometric correlation gives $\tan(\theta_j/2)=R_{\rm jet}/R_{\rm GRB}$, and combining Eq. (24), therefore,

$$S_{\rm jet} \propto R_{\rm GRB}^2 \propto \begin{cases} (\Gamma^{-2/3})^2 \propto \Gamma^{-4/3} \propto t^{1/2}, & \text{ISM} \\ (\Gamma^{-2})^2 \propto \Gamma^{-4} \propto t^1, & \text{wind}, \\ (\Gamma^{-1/3})^2 \propto \Gamma^{-2/3} \propto t^{2/7}, & \text{Radiative fireball}, \\ (\Gamma^{-6/5})^2 \propto \Gamma^{-12/5} \propto t^{3/4}, & \text{Energy injection} \end{cases} \tag{26}$$

Before the jet break effect $t \lesssim t_{\rm jet}$, the observed area is $S_{\rm obs}$ on the jet plane and $\pi_{\rm obs} \propto S_{\rm obs}^{-1}$, one therefore has

$$\pi_{\rm obs} \propto S_{\rm obs}^{-1} \propto \Gamma^2 \propto \begin{cases} t^{-3/4}, & \text{ISM} \\ t^{-1/2}, & \text{wind}, \\ t^{-6/7}, & \text{Radiative fireball}, \\ t^{-5/8}, & \text{Energy injection} \end{cases} \tag{27}$$

After the jet break effect $t \gtrsim t_{\rm jet}$, the observed area $S_{\rm obs}$ is larger than the total emission area $S_{\rm jet}$. The total net polarization degree $\pi_{\rm obs}$ has been accounted, thus approximately remains as a constant or slowly decreases in time.

A possible test can be made by investigating the $\pi_{\rm obs}$-$\Gamma(\pi)$ relation via observational data, where $\Gamma(\pi)$ is the bulk Lorentz factor measured during the epoch of polarization. Two main methods have been proposed to estimate Γ of a GRB fireball from the literature[11,30], either using a thermal component from prompt emission spectra[30] or using the early afterglow light curves that

show the signal of fireball deceleration[11]. The former one may not be universally applicable since thermal component spectra have only been observed in a handful of *Fermi*-detected GRBs to date. We therefore focus on the latter one. Additionally, $\Gamma(\pi)$ cannot be precisely estimated in many bursts due to their polarization being measured in various emission regions (some in early prompt emission, some others in late after emission). As a proxy of $\Gamma(\pi)$, we use the initial Lorentz factor Γ_0 (at the deceleration radius of the GRBs), which can be estimated by using an empirical relation[11] ($\Gamma_0 \simeq 249 L_{\gamma,\rm iso,52}^{0.30}$), where $L_{\gamma,\rm iso}$ is the average isotropic-equivalent luminosity during prompt emission phase. In order to obtain $L_{\gamma,\rm iso}$, we perform time-integrated spectral analysis of the prompt emission for each burst, following the standard practices[31,32] used by the full Python package, namely, the Multi-Mission Maximum Likelihood Framework (3ML[33]). The energy flux F_γ (erg cm^{-2}s^{-1}) can therefore be obtained from the spectral fit, with a k-correction (k_c) applied. With F_γ and redshift measurements, one can estimate the average isotropic-equivalent luminosity $L_{\gamma,\rm iso} = 4\hat{\pi} d_L^2 F_\gamma k_c$.

Extended Data Figure 6 shows the $\pi_{\rm obs}$-Γ_0 correlation. We note that for those bursts in which the polarization is measured during the prompt emission phase, one has $\Gamma_0 < \Gamma(\pi)$ due to $t_{\Gamma_0} < t_{\Gamma(\pi)}$ (see the data points in Extended Data Figure 6 with rightward arrows). While the polarization for the remaining GRBs is measured in the optical band during afterglow emission and has $t_{\Gamma_0} > t_{\Gamma(\pi)}$, one therefore has $\Gamma_0 > \Gamma(\pi)$ (see the data points in Figure 6 with leftward arrows). In summary, the data points are clustered around the solid line defined by the function $\pi_{\rm obs} \propto \Gamma^2$ (see the solid line in Figure 6), which strongly supports our explanations.

We show that the GRB polarization degrees ($\pi_{\rm obs}$) decay as a power-law over time, which takes the form of $\pi_{\rm obs} \propto t^{-0.50\pm0.02}$ (Figure 1) and the theoretical explanation $\pi_{\rm obs} \propto S_{\rm obs}^{-1} \propto \Gamma^2$ (Eq.27), which is verified by the $\pi_{\rm obs} - \Gamma$ relation (Figure 6) from data. As a result, using afterglow models of time-decaying Lorentz factors $\Gamma \propto t^{-\alpha/2}$ (Eq.24), we obtain the polarization scaling law $\pi_{\rm obs} \propto t^{-\alpha}$. Therefore, the obtained power-law index of polarization ($\alpha_{\rm obs}$=-0.50 $\pm$ 0.02) from the time-integrated polarization sample can be used as a probe for further information constraints of the afterglow models and environment surrounding GRBs (Extended Data Figure 7).

Searching for a jet break in the afterglow lightcurve (Segment III) A bit-increment polarization data (deviating from the main power-law function) around 10^4 to 10^5 seconds were observed in 5 GRBs (GRB 990510, GRB 010222, GRB 020405, GRB 030328, and GRB 080928, see Figure 1). In the presented scenario, these observed properties are naturally explained as the "jet break" boundary effects that non-axial symmetric irregularities on jet-plan boundary are seen and effective magnetic patch area $S_{\rm patch}^{\rm eff}$ increases in Eq.(5). To verify such an explanation, we further analyse their afterglow lightcurves. This is because the afterglow lightcurves are usually characterized by a post-jet break when the jet boundary is observed, with a steeper temporal decay slope ($\alpha \sim p > 1.5$, Ref.[25]) than normal decay, where p is the electron spectral distribution index. As a result shown in the left panel of Extended Data Figure 8, it is clearly evident that in these four GRB events, net ploarization increment and afterglow lightcurve decrement are indeed correlated at jet break time.

Extended Data Figure 8 shows the optical afterglow lightcurves for these five bursts and their

polarization data. We fit these lightcurves using a BKPL/SPL model, and pay special attention to their break time (if any) and post-break slope. The best fit results are summarized in Table 4. We find that four out of five bursts have post-break slopes larger than 1.5, which can be accounted for by the jet-break phenomenon. In addition, the post-break times measured from the fitting (with uncertainties) of three bursts (GRB 990510, GRB 010222, and GRB 030328) overlap with the epochs of their polarization observations.

References

1. Blandford, R. D. & Znajek, R. L. Electromagnetic extraction of energy from Kerr black holes. *mnras* **179**, 433–456 (1977).

2. Thompson, C. A Model of Gamma-Ray Bursts. *mnras* **270**, 480 (1994).

3. Spruit, H. C., Daigne, F. & Drenkhahn, G. .

4. Lyutikov, M. & Blandford, R. Gamma Ray Bursts as Electromagnetic Outflows. *arXiv Astrophysics e-prints* (2003). astro-ph/0312347.

5. Dai, Z. G., Wang, X. Y., Wu, X. F. & Zhang, B. X-ray Flares from Postmerger Millisecond Pulsars. *Science* **311**, 1127–1129 (2006). astro-ph/0602525.

6. Ruffini, R., Vereshchagin, G. & Xue, S.-S. Electron-positron pairs in physics and astrophysics: From heavy nuclei to black holes. *Phys. Rep.* **487**, 1–140 (2010). 0910.0974.

7. Li, L. *et al.* Constraining the Type of Central Engine of GRBs with Swift Data. *Astrophys. J., Suppl.* **236**, 26 (2018). 1712.09390.

8. Xue, S.-S. Gravo-thermal catastrophe in gravitational collapse and energy progenitor of Gamma-Ray Bursts. *J. Cosm. and Astro. Phys.* **2021**, 044 (2021). 2104.03021.

9. Rybicki, G. B. & Lightman, A. P. *Radiative processes in astrophysics* (1979).

10. De Angelis, N. *et al.* Development and science perspectives of the POLAR-2 instrument: a large scale GRB polarimeter. *arXiv e-prints* arXiv:2109.02978 (2021). 2109.02978.

11. Lü, J. *et al.* Lorentz-factor-Isotropic-luminosity/Energy Correlations of Gamma-Ray Bursts and Their Interpretation. *Astrophys. J.* **751**, 49 (2012). 1109.3757.

12. Liang, E.-W. *et al.* Constraining Gamma-ray Burst Initial Lorentz Factor with the Afterglow Onset Feature and Discovery of a Tight $\Gamma_0 - E_{\gamma,iso}$ Correlation. *Astrophys. J.* **725**, 2209–2224 (2010). 0912.4800.

13. Granot, J., Nakar, E. & Piran, T. Astrophysics: refreshed shocks from a γ-ray burst. *Nature* **426**, 138–139 (2003). astro-ph/0304563.

14. Sagiv, A., Waxman, E. & Loeb, A. Probing the Magnetic Field Structure in Gamma-Ray Bursts through Dispersive Plasma Effects on the Afterglow Polarization. *Astrophys. J.* **615**, 366–377 (2004). astro-ph/0401620.

15. Lundman, C., Vurm, I. & Beloborodov, A. M. Polarization of gamma-ray bursts in the dissipative photosphere model. *Astrophys. J.* **856**, 145 (2018). 1611.01451.

16. Rees, M. J. & Mészáros, P. Dissipative Photosphere Models of Gamma-Ray Bursts and X-Ray Flashes. *Astrophys. J.* **628**, 847–852 (2005). astro-ph/0412702.

17. Pe'er, A., Mészáros, P. & Rees, M. J. The Observable Effects of a Photospheric Component on GRB and XRF Prompt Emission Spectrum. *Astrophys. J.* **642**, 995–1003 (2006). astro-ph/0510114.

18. Amati, L. *et al.* Intrinsic spectra and energetics of BeppoSAX Gamma-Ray Bursts with known redshifts. *Astron. Astrophys.* **390**, 81–89 (2002). astro-ph/0205230.

19. Gill, R., Granot, J. & Kumar, P. Linear polarization in gamma-ray burst prompt emission. *mnras* **491**, 3343–3373 (2020). 1811.11555.

20. Lazzati, D., Rossi, E., Ghisellini, G. & Rees, M. J. Compton drag as a mechanism for very high linear polarization in gamma-ray bursts. *mnras* **347**, L1–L5 (2004). astro-ph/0309038.

21. Zhang, S., Jin, Z.-P. & Wei, D.-M. The Magnetization Degree of the Outflow Powering the Highly Polarized Reverse-shock Emission of GRB 120308A. *Astrophys. J.* **798**, 3 (2015). 1407.6430.

22. Mundell, C. G. *et al.* Highly polarized light from stable ordered magnetic fields in GRB 120308A. *Nature* **504**, 119–121 (2013).

23. Salvatier, J., Wieckiâ, T. V. & Fonnesbeck, C. PyMC3: Python probabilistic programming framework. Astrophysics Source Code Library, record ascl:1610.016 (2016). 1610.016.

24. Chib, S. Chapter 57 - markov chain monte carlo methods: Computation and inference. vol. 5 of *Handbook of Econometrics*, 3569–3649 (Elsevier, 2001). URL https://www.sciencedirect.com/science/article/pii/S1573441201050103.

25. Rhoads, J. E. The Dynamics and Light Curves of Beamed Gamma-Ray Burst Afterglows. *Astrophys. J.* **525**, 737–749 (1999). astro-ph/9903399.

26. Woosley, S. Astronomy: Blinded by the light. *Nature* **414**, 853–854 (2001).

27. Zhang, B. *The Physics of Gamma-Ray Bursts* (2018).

28. Chevalier, R. A. & Li, Z.-Y. Gamma-Ray Burst Environments and Progenitors. *Astrophys. J. Lett.* **520**, L29–L32 (1999). astro-ph/9904417.

29. Zhang, B. & Mészáros, P. Gamma-Ray Burst Afterglow with Continuous Energy Injection: Signature of a Highly Magnetized Millisecond Pulsar. *Astrophys. J. Lett.* **552**, L35–L38 (2001). astro-ph/0011133.

30. Pe'er, A., Ryde, F., Wijers, R. A. M. J., Mészáros, P. & Rees, M. J. A New Method of Determining the Initial Size and Lorentz Factor of Gamma-Ray Burst Fireballs Using a Thermal Emission Component. *Astrophys. J. Lett.* **664**, L1–L4 (2007). astro-ph/0703734.

31. Yu, H.-F., Dereli-Bégué, H. & Ryde, F. Bayesian Time-resolved Spectroscopy of GRB Pulses. *Astrophys. J.* **886**, 20 (2019). 1810.07313.

32. Li, L., Ryde, F., Pe'er, A., Yu, H.-F. & Acuner, Z. Bayesian Time-resolved Spectroscopy of Multipulse GRBs: Variations of Emission Properties among Pulses. *Astrophys. J., Suppl.* **254**, 35 (2021). 2012.03038.

33. Vianello, G. *et al.* The Multi-Mission Maximum Likelihood framework (3ML). *arXiv e-prints* (2015). 1507.08343.

34. Willis, D. R. *et al.* Evidence of polarisation in the prompt gamma-ray emission from GRB 930131 and GRB 960924. *Astron. Astrophys.* **439**, 245–253 (2005). astro-ph/0505097.

35. Taylor, G. B. *et al.* The Discovery of the Radio Afterglow from the Optically DIM Gamma-Ray Burst of 1998 March 29. *Astrophys. J. Lett.* **502**, L115–L118 (1998). astro-ph/9805333.

36. Patat, F. *et al.* The Metamorphosis of SN 1998bw. *Astrophys. J.* **555**, 900–917 (2001). astro-ph/0103111.

37. Kay, L. E. *et al.* Supernova 1998bw in ESO 184-G82. *IAU Circ.* **6969**, 1 (1998).

38. Hjorth, J. *et al.* Polarimetric Constraints on the Optical Afterglow Emission from GRB 990123. *Science* **283**, 2073 (1999).

39. Kulkarni, S. R. *et al.* Discovery of a Radio Flare from GRB 990123. *Astrophys. J. Lett.* **522**, L97–L100 (1999). astro-ph/9903441.

40. Wijers, R. A. M. J. *et al.* Detection of Polarization in the Afterglow of GRB 990510 with the ESO Very Large Telescope. *Astrophys. J. Lett.* **523**, L33–L36 (1999). astro-ph/9906346.

41. Rol, E. *et al.* GRB 990712: First Indication of Polarization Variability in a Gamma-Ray Burst Afterglow. *Astrophys. J.* **544**, 707–711 (2000). astro-ph/0007015.

42. Covino, S., Ghisellini, G., Lazzati, D. & Malesani, D. Polarization of Gamma-Ray Burst Optical and Near-Infrared Afterglows. In Feroci, M., Frontera, F., Masetti, N. & Piro, L. (eds.) *Gamma-Ray Bursts in the Afterglow Era*, vol. 312 of *Astronomical Society of the Pacific Conference Series*, 169 (2004). astro-ph/0301608.

43. Stecklum, B., Fischer, O., Klose, S., Mundt, R. & Bailer-Jones, C. Near-infrared polarimetric observations of the afterglow of GRB 000301C. In Wheeler, J. C. & Martel, H. (eds.) *20th Texas Symposium on relativistic astrophysics*, vol. 586 of *American Institute of Physics Conference Series*, 635–637 (2001). astro-ph/0103120.

44. Björnsson, G., Hjorth, J., Pedersen, K. & Fynbo, J. U. The Afterglow of GRB 010222: A Case of Continuous Energy Injection. *Astrophys. J. Lett.* **579**, L59–L62 (2002). astro-ph/0209585.

45. Covino, S. *et al.* Polarimetric observations of GRB 011211. *Astron. Astrophys.* **392**, 865–868 (2002). astro-ph/0207335.

46. Masetti, N. *et al.* Optical and near-infrared observations of the GRB020405 afterglow. *Astron. Astrophys.* **404**, 465–481 (2003). astro-ph/0302350.

47. Bersier, D. *et al.* The Strongly Polarized Afterglow of GRB 020405. *Astrophys. J. Lett.* **583**, L63–L66 (2003). astro-ph/0206465.

48. Covino, S. *et al.* Polarization evolution of the GRB 020405 afterglow. *Astron. Astrophys.* **400**, L9–L12 (2003). astro-ph/0211245.

49. Barth, A. J. *et al.* Optical Spectropolarimetry of the GRB 020813 Afterglow. *Astrophys. J. Lett.* **584**, L47–L51 (2003). astro-ph/0212554.

50. Covino, S. *et al.* GRB 020813: addendum to GCN 1498. *GRB Coordinates Network* **1502**, 1 (2002).

51. Gorosabel, J. *et al.* GRB 020813: Polarization in the case of a smooth optical decay. *Astron. Astrophys.* **422**, 113–119 (2004). astro-ph/0309748.

52. Rol, E. *et al.* Variable polarization in the optical afterglow of GRB 021004. *Astron. Astrophys.* **405**, L23–L27 (2003). astro-ph/0305227.

53. Lazzati, D. *et al.* Intrinsic and dust-induced polarization in gamma-ray burst afterglows: The case of GRB 021004. *Astron. Astrophys.* **410**, 823–831 (2003). astro-ph/0308540.

54. Rutledge, R. E. & Fox, D. B. Re-analysis of polarization in the γ-ray flux of GRB 021206. *mnras* **350**, 1288–1300 (2004). astro-ph/0310385.

55. Wigger, C., Hajdas, W., Arzner, K., Güdel, M. & Zehnder, A. Gamma-Ray Burst Polarization: Limits from RHESSI Measurements. *Astrophys. J.* **613**, 1088–1100 (2004). astro-ph/0405525.

56. Klose, S. *et al.* Probing a Gamma-Ray Burst Progenitor at a Redshift of z = 2: A Comprehensive Observing Campaign of the Afterglow of GRB 030226. *Astrophys. J.* **128**, 1942–1954 (2004). astro-ph/0408041.

57. Maiorano, E. *et al.* Physics of the GRB 030328 afterglow and its environment. *Astron. Astrophys.* **455**, 423–431 (2006). astro-ph/0604093.

58. Greiner, J. *et al.* Evolution of the polarization of the optical afterglow of the γ-ray burst GRB030329. *Nature* **426**, 157–159 (2003). astro-ph/0311282.

59. Klose, S. *et al.* Prospects for multiwavelength polarization observations of GRB afterglows and the case GRB 030329. *Astron. Astrophys.* **420**, 899–903 (2004). astro-ph/0403504.

60. Magalhaes, A. M., Pereyra, A., Dominici, T. & Abraham, Z. GRB030329: optical polarization. *GRB Coordinates Network* **2163**, 1 (2003).

61. Taylor, G. B., Frail, D. A., Berger, E. & Kulkarni, S. R. The Angular Size and Proper Motion of the Afterglow of GRB 030329. *Astrophys. J. Lett.* **609**, L1–L4 (2004). astro-ph/0405300.

62. Taylor, G. B., Momjian, E., Pihlström, Y., Ghosh, T. & Salter, C. Late-Time Observations of the Afterglow and Environment of GRB 030329. *Astrophys. J.* **622**, 986–990 (2005). astro-ph/0412483.

63. Kalemci, E., Boggs, S. E., Kouveliotou, C., Finger, M. & Baring, M. G. Search for Polarization from the Prompt Gamma-Ray Emission of GRB 041219a with SPI on INTEGRAL. *Astrophys. J., Suppl.* **169**, 75–82 (2007). astro-ph/0610771.

64. McGlynn, S. *et al.* Polarisation studies of the prompt gamma-ray emission from GRB 041219a using the spectrometer aboard INTEGRAL. *Astron. Astrophys.* **466**, 895–904 (2007). astro-ph/0702738.

65. Götz, D., Laurent, P., Lebrun, F., Daigne, F. & Bošnjak, Ž. Variable Polarization Measured in the Prompt Emission of GRB 041219A Using IBIS on Board INTEGRAL. *Astrophys. J. Lett.* **695**, L208–L212 (2009). 0903.1712.

66. McGlynn, S. *et al.* High energy emission and polarisation limits for the INTEGRAL burst GRB 061122. *Astron. Astrophys.* **499**, 465–472 (2009). 0903.5218.

67. Götz, D., Covino, S., Fernández-Soto, A., Laurent, P. & Bošnjak, Ž. The polarized gamma-ray burst GRB 061122. *mnras* **431**, 3550–3556 (2013). 1303.4186.

68. Covino, S. *et al.* The complex light curve of the afterglow of GRB071010A. *mnras* **388**, 347–356 (2008). 0804.4367.

69. Littlejohns, O. M. *et al.* The origin of the early-time optical emission of Swift GRB 080310. *mnras* **421**, 2692–2712 (2012). 1201.1292.

70. Covino, S. & Gotz, D. Polarization of prompt and afterglow emission of Gamma-Ray Bursts. *Astronomical and Astrophysical Transactions* **29**, 205–244 (2016). 1605.03588.

71. Steele, I. A., Mundell, C. G., Smith, R. J., Kobayashi, S. & Guidorzi, C. Ten per cent polarized optical emission from GRB090102. *Nature* **462**, 767–769 (2009). 1010.1255.

72. Wiersema, K. *et al.* Detailed optical and near-infrared polarimetry, spectroscopy and broadband photometry of the afterglow of GRB 091018: polarization evolution. *mnras* **426**, 2–22 (2012). 1203.4265.

73. Uehara, T. *et al.* GRB 091208B: First Detection of the Optical Polarization in Early Forward Shock Emission of a Gamma-Ray Burst Afterglow. *Astrophys. J. Lett.* **752**, L6 (2012). 1205.2149.

74. Yonetoku, D. *et al.* Detection of Gamma-Ray Polarization in Prompt Emission of GRB 100826A. *Astrophys. J. Lett.* **743**, L30 (2011). 1111.1779.

75. Gorbovskoy, E. S. *et al.* Prompt, early and afterglow optical observations of five γ-ray bursts: GRB 100901A, GRB 100902A, GRB 100905A, GRB 100906A and GRB 101020A. *mnras* **421**, 1874–1890 (2012). 1111.3625.

76. Gorosabel, J., Duffard, R., Kubanek, P. & Guijarro, A. GRB 110205A: detection of optical linear polarization from CAHA. *GRB Coordinates Network* **11696**, 1 (2011).

77. Cucchiara, A. *et al.* Constraining Gamma-Ray Burst Emission Physics with Extensive Early-time, Multiband Follow-up. *Astrophys. J.* **743**, 154 (2011). 1107.3352.

78. Yonetoku, D. *et al.* Magnetic Structures in Gamma-Ray Burst Jets Probed by Gamma-Ray Polarization. *Astrophys. J. Lett.* **758**, L1 (2012). 1208.5287.

79. Pruzhinskaya, M. V. *et al.* Optical polarization observations with the MASTER robotic net. *N. Astro.* **29**, 65–74 (2014). 1401.3221.

80. Wiersema, K. *et al.* Circular polarization in the optical afterglow of GRB 121024A. *Nature* **509**, 201–204 (2014). 1410.0489.

81. van der Horst, A. J. *et al.* A comprehensive radio view of the extremely bright gamma-ray burst 130427A. *mnras* **444**, 3151–3163 (2014). 1404.1945.

82. King, O. G. *et al.* Early-time polarized optical light curve of GRB 131030A. *mnras* **445**, L114–L118 (2014). 1409.2417.

83. Götz, D. *et al.* GRB 140206A: the most distant polarized gamma-ray burst. *mnras* **444**, 2776–2782 (2014). 1408.4121.

84. Kopač, D. *et al.* Limits on Optical Polarization during the Prompt Phase of GRB 140430A. *Astrophys. J.* **813**, 1 (2015). 1509.03099.

85. Gorbovskoy, E. S. *et al.* Early polarization observations of the optical emission of gamma-ray bursts: GRB 150301B and GRB 150413A. *mnras* **455**, 3312–3318 (2016). 1511.02641.

86. Lowell, A. W. *et al.* Polarimetric Analysis of the Long Duration Gamma Ray Burst GRB 160530A With the Balloon Borne Compton Spectrometer and Imager. *Astrophys. J.* **848**, 119 (2017). 1709.05349.

87. Troja, E. *et al.* Significant and variable linear polarization during the prompt optical flash of GRB 160625B. *Nature* **547**, 425–427 (2017).

88. Chand, V. *et al.* Violation of Synchrotron Line of Death by the Highly Polarized GRB 160802A. *Astrophys. J.* **862**, 154 (2018). 1806.06847.

89. Sharma, V. *et al.* Time-varying Polarized Gamma-Rays from GRB 160821A: Evidence for Ordered Magnetic Fields. *Astrophys. J. Lett.* **882**, L10 (2019). 1908.10885.

90. Kole, M. *et al.* The POLAR gamma-ray burst polarization catalog. *Astron. Astrophys.* **644**, A124 (2020). 2009.04871.

91. Corsi, A. *et al.* An upper-limit on the linear polarization fraction of the GW170817 radio continuum. *Astrophys. J.* **861**, L10 (2018). 1806.03136.

92. Chand, V. *et al.* AstroSat-CZTI Detection of Variable Prompt Emission Polarization in GRB 171010A. *Astrophys. J.* **874**, 70 (2019). 1807.01737.

93. Urata, Y. *et al.* First Detection of Radio Linear Polarization in a Gamma-Ray Burst Afterglow. *Astrophys. J. Lett.* **884**, L58 (2019). 1904.08111.

94. Laskar, T. *et al.* ALMA Detection of a Linearly Polarized Reverse Shock in GRB 190114C. *Astrophys. J. Lett.* **878**, L26 (2019). 1904.07261.

95. Jordana-Mitjans, N. *et al.* Lowly Polarized Light from a Highly Magnetized Jet of GRB 190114C. *Astrophys. J.* **892**, 97 (2020). 1911.08499.

96. Gupta, R. *et al.* Probing into emission mechanisms of GRB 190530A using time-resolved spectra and polarization studies: Synchrotron Origin? *mnras* (2022). 2201.01167.

97. Shrestha, M. *et al.* GRB 191016A: A highly collimated gamma-ray burst jet with magnetised energy injection. *arXiv e-prints* arXiv:2111.09123 (2021). 2111.09123.

Extended Data

1. Extended Data Figure 1: **The degree of polarization ($\pi_{\rm obs}$) in a time-integrated manner is plotted as a function of their time intervals after the burst at the cosmological distance.**

2. Extended Data Figure 2: **Upper panel (a): a sketch plot for delineating the correlation between GRB polarization and the Lorentz factor. We consider a conical jet with line-of-sight aligned with the jet axis with a jet opening angle θ_j(=$\angle$HAD). Assuming that A is the GRB central engine, B is the observer, O is the center point of the plane, C(G) are the highest latitude photons on the conical jet that the relativistic emission can be observed by the observer, and D (H) are the boundary of the conical jet on the plane. Due to relativistic beaming, the relativistic emission produced by the photon C can be observed only inside the cone θ_e ($\angle$ BCF). Lower panel (b): same as (a) but considering a conical jet with line-of-sight unaligned with the jet axis.**

3. Extended Data Figure 5: **A cartoon picture for "magnetic patches" on the jet plane represented by many small circles with random red arrows; the observed area $S_{\rm obs} \propto 1/\Gamma^2$ increase in time represented by four hollow circles corresponding to the hollow circles in Fig.2; the irregular jet boundary represented by a waved circle.**

4. Extended Data Figure 3: **The numbers $N_{\rm p}$(=$S_{\rm obs}/S_{\rm patch}$:cyan line), $N_{\rm patch}$(=$S_{\rm jet}/S_{\rm patch}$:yellow line), and $N_{\rm obs}$(=$S_{\rm jet}/S_{\rm obs}$:grey line) as functions of rest-frame time, as well as their typical values (indicated by different colored data points). Data points colored by green and magenta indicate $t_{\rm obs}=t_{\rm patch}$ and $t_{\rm obs}=t_{\rm jet}$, respectively. $N_{\rm p}$: when $t_{\rm obs}\lesssim t_{\rm patch}$, one has $S_{\rm obs}\lesssim S_{\rm patch}$, and $N_{\rm p}\lesssim 1$; when $t_{\rm patch}\lesssim t_{\rm obs}\lesssim t_{\rm jet}$, one has $S_{\rm patch}\lesssim S_{\rm obs}\lesssim S_{\rm jet}$, and $N_{\rm p}\gtrsim 1$ follows a rapidly rising scaling law over time (cyan line); when $t_{\rm obs}\gtrsim t_{\rm jet}$, one has $S_{\rm obs}\gtrsim S_{\rm jet}$ and $N_{\rm p}$ follows a slowly rising scaling law over time (yellow). $N_{\rm patch}$: compared with $N_{\rm p}$, $N_{\rm patch}$ follows a slowly rising scaling law (note that we have assumed typical observed parameters: $N_{\rm patch}$=600 at the $\Pi_{\rm max}$ point and $N_{\rm patch}$=900 at the jet break time) over time when $t_{\rm obs}\lesssim t_{\rm jet}$. However, $N_{\rm p}$ and $N_{\rm patch}$ will share the same scaling law, when $t_{\rm obs}\gtrsim t_{\rm jet}$. $N_{\rm obs}$: given the typical initial observed parameters (e.g., $N_{\rm obs}$=900, see Methods), $N_{\rm obs}$ as a function of time can be described by the orange line. Note that: one has $N_{\rm obs}\approx 1$, when $t\gtrsim t_{\rm jet}$. Summarized information is given in Table 3.**

5. Extended Data Figure 4: **The numbers $N_{\rm p}$, $N_{\rm patch}$, and $N_{\rm obs}$ depend on Γ^2. By assuming typical values (e.g., $N_{\rm patch}$=900 when Γ=300) and a typical jet opening angle (θ_j=0.1) measured from GRBs, $N_{\rm p}$, $N_{\rm patch}$, and $N_{\rm obs}$ as functions of Γ can be described by the cyan (Eq.19), grey (Eq.20), and yellow (Eq.9) lines. The data points with different colors represent several typical Γ values and their corresponding N values. For example, when $\Gamma=300$ (at $\Pi_{\rm max}$ point), one has $N_{\rm p}=1$, $N_{\rm patch}=900$, and $N_{\rm obs}=900$; when $\Gamma=10$ (at jet break time); $N_{\rm p}=900$, $N_{\rm patch}=900$ and $N_{\rm obs}=1$; and when $\Gamma=1$, one has $N_{\rm p}=900$, $N_{\rm patch}=900$, and $N_{\rm obs}=1$. Note that (i) when $\Gamma=1$, $N_{\rm obs}=1$, rather than $N_{\rm obs}=0.01$ due to the "jet break" boundary effect; (ii) when $\Gamma\lesssim 10$ ($t_{\rm obs}\gtrsim t_{\rm jet}$), $N_{\rm p}$ and $N_{\rm patch}$ share the same function (dashed line). Summarized information is given in Table 3.**

6. Extended Data Figure 5: **The solid line is qualitatively illustrated by the time evolution of $S^{\rm eff}_{\rm patch}/S_{\rm patch}$, while the data points with purple and orange colors indicate the $\Pi_{\rm max}$ point and the typical jet break time.**

7. Extended Data Figure 6: **Time-integrated degrees of polarization $\pi_{\rm obs}$ as a function of the initial Lorentz factor Γ_0 at the deceleration radius, where Γ_0 is estimated by the empirical relation ($\Gamma_0\simeq 249 L^{0.30}_{\gamma,{\rm iso},52}$). The solid lines represent the functions of $\pi_{\rm obs}\propto\Gamma^2$. The rightward ($\Gamma_0<\Gamma_\pi$: prompt emission phase) and leftward ($\Gamma_0>\Gamma_\pi$: afterglow emission phase) arrows represent the region in which the bulk Lorentz factor is measured during the epoch of polarization.**

8. Extended Data Figure 7: **Comparing various afterglow models with observed results in the $\pi_{\rm obs}$-[t/(1+z)] plane. The solid line is the best fits using the power-law model from**

the observational data and with 2σ (95% confidence interval) error shadow region. The solid lines indicated by different colors represent different afterglow models.

9. Extended Data Figure 8: **Optical (R-band) afterglow lightcurves (dotted lines) (left panel) and the degree of polarization (right panel) for the five bursts that have a jet break around the polarization epoch. (GRB 990510, GRB 010222, GRB 020405, GRB 030328, and GRB 080928). The dashed lines in left panel represent the best fits using a BKPL/SPL model.**

10. Extended Data Table 1: **A full catalog of GRB polarimetric observations.**

11. Extended Data Table 4: **Fit Results for the Optical Afterglow Lightcurve (Jet Breaks).**

12. Extended Data Table 5: **Results of Inferred Γ_0.**

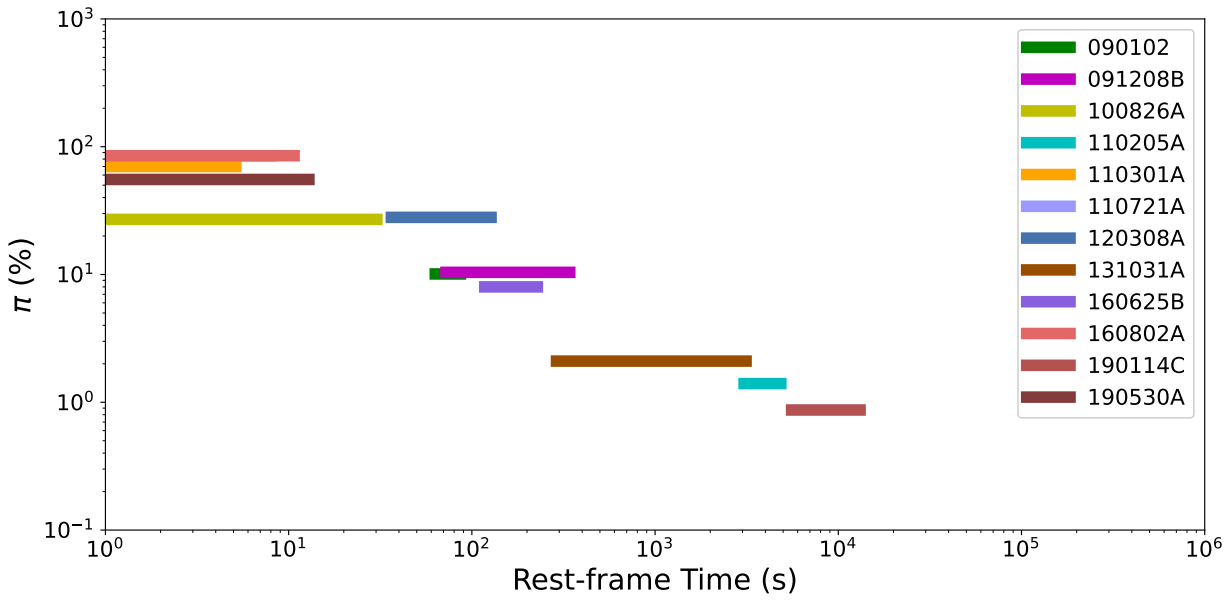

Figure 1: The degree of polarization ($\pi_{\rm obs}$) in a time-integrated manner is plotted as a function of their time intervals after the burst at the cosmological distance.

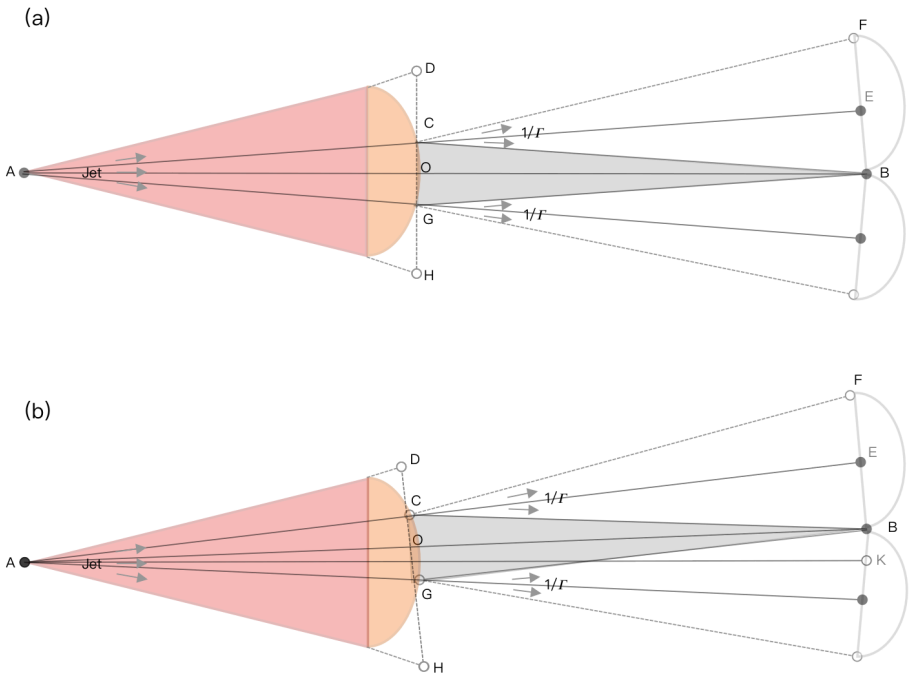

Figure 2: Upper panel (a): a sketch plot for delineating the correlation between GRB polarization and the Lorentz factor. We consider a conical jet with line-of-sight aligned with the jet axis with a jet opening angle θ_j(=$\angle$HAD). Assuming that A is the GRB central engine, B is the observer, O is the center point of the plane, C(G) are the highest latitude photons on the conical jet that the relativistic emission can be observed by the observer, and D (H) are the boundary of the conical jet on the plane. Due to relativistic beaming, the relativistic emission produced by the photon C can be observed only inside the cone θ_e ($\angle$ BCF). Lower panel (b): same as (a) but considering a conical jet with line-of-sight unaligned with the jet axis.

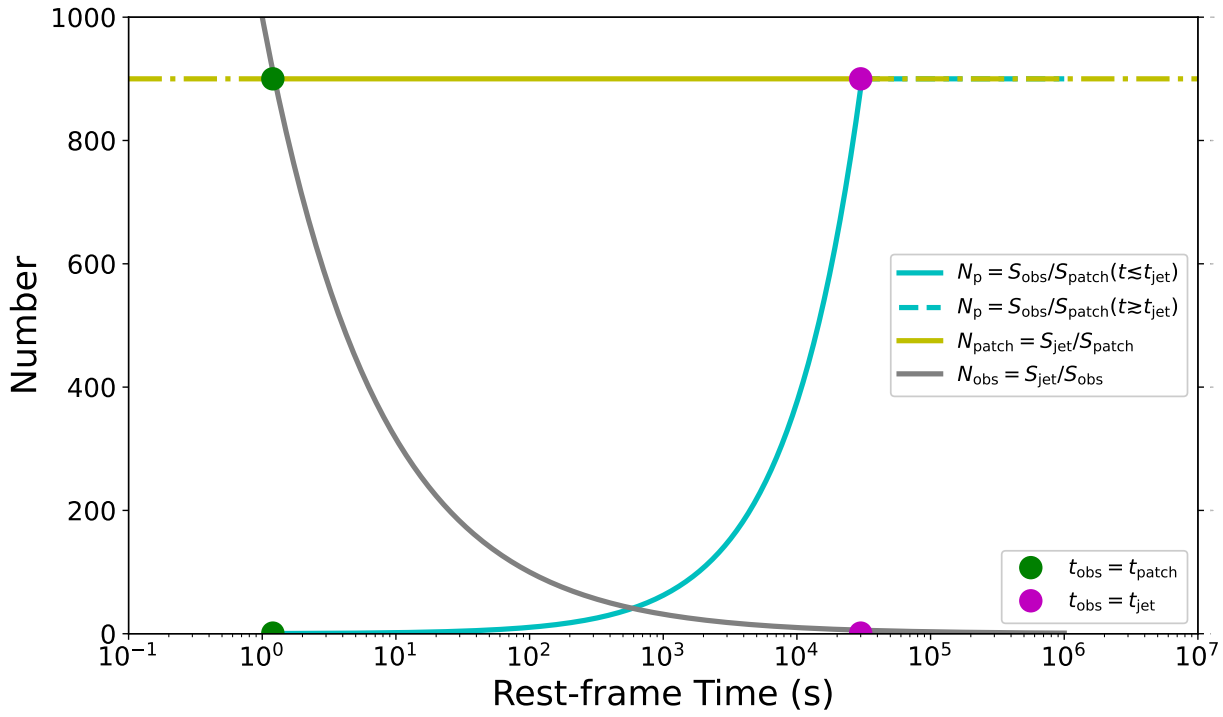

Figure 3: The numbers $N_{\rm p}$(=$S_{\rm obs}/S_{\rm patch}$:cyan line), $N_{\rm patch}$(=$S_{\rm jet}/S_{\rm patch}$:yellow line), and $N_{\rm obs}$(=$S_{\rm jet}/S_{\rm obs}$:grey line) as functions of rest-frame time, as well as their typical values (indicated by different colored data points). Data points colored by green and magenta indicate $t_{\rm obs} = t_{\rm patch}$ and $t_{\rm obs} = t_{\rm jet}$, respectively. $N_{\rm p}$: when $t_{\rm obs} \lesssim t_{\rm patch}$, one has $S_{\rm obs} \lesssim S_{\rm patch}$, and $N_{\rm p} \lesssim 1$; when $t_{\rm patch} \lesssim t_{\rm obs} \lesssim t_{\rm jet}$, one has $S_{\rm patch} \lesssim S_{\rm obs} \lesssim S_{\rm jet}$, and $N_{\rm p} \gtrsim 1$ follows a rapidly rising scaling law over time (cyan line); when $t_{\rm obs} \gtrsim t_{\rm jet}$, one has $S_{\rm obs} \gtrsim S_{\rm jet}$ and $N_{\rm p}$ follows a slowly rising scaling law over time (yellow). $N_{\rm patch}$: compared with $N_{\rm p}$, $N_{\rm patch}$ follows a slowly rising scaling law (note that we have assumed typical observed parameters: $N_{\rm patch}$=900 at the $\Pi_{\rm max}$ point and $N_{\rm patch}$=900 at the jet break time) over time when $t_{\rm obs} \lesssim t_{\rm jet}$. However, $N_{\rm p}$ and $N_{\rm patch}$ will share the same scaling law, when $t_{\rm obs} \gtrsim t_{\rm jet}$. $N_{\rm obs}$: given the typical initial observed parameters (e.g., $N_{\rm obs}$=900, see Methods), $N_{\rm obs}$ as a function of time can be described by the orange line. Note that: one has $N_{\rm obs} \approx 1$, when $t \gtrsim t_{\rm jet}$. Summarized information is given in Table 3.

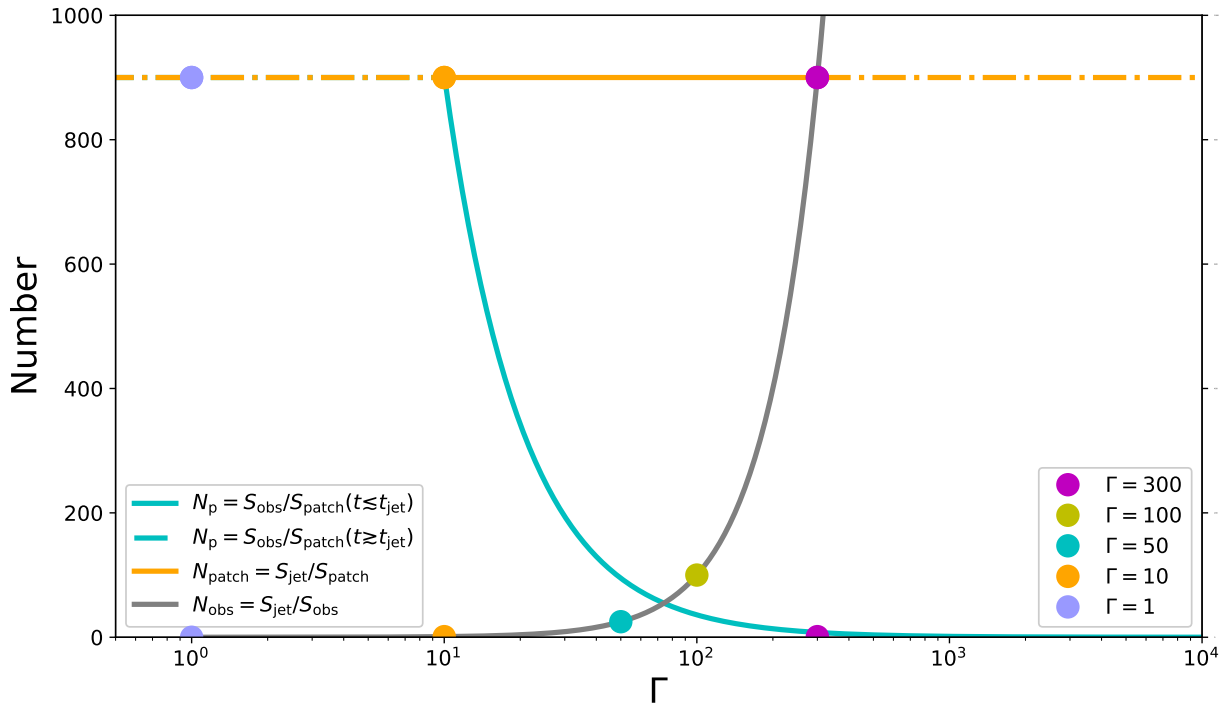

Figure 4: The numbers $N_{\rm p}$, $N_{\rm patch}$, and $N_{\rm obs}$ depend on Γ^2. By assuming typical values (e.g., $N_{\rm patch}$=900 when Γ=300) and a typical jet opening angle (θ_j=0.1) measured from GRBs, $N_{\rm p}$, $N_{\rm patch}$, and $N_{\rm obs}$ as functions of Γ can be described by the cyan (Eq.19), grey (Eq.20), and yellow (Eq.9) lines. The data points with different colors represent several typical Γ values and their corresponding N values. For example, when $\Gamma = 300$ (at $\Pi_{\rm max}$ point), one has $N_{\rm p} = 1$, $N_{\rm patch} = 900$, and $N_{\rm obs} = 900$; when $\Gamma = 10$ (at jet break time); $N_{\rm p} = 900$, $N_{\rm patch} = 900$ and $N_{\rm obs} = 1$; and when $\Gamma = 1$, one has $N_{\rm p} = 900$, $N_{\rm patch} = 900$, and $N_{\rm obs} = 1$. Note that (i) when $\Gamma = 1$, $N_{\rm obs} = 1$, rather than $N_{\rm obs} = 0.01$ due to the "jet break" boundary effect; (ii) when $\Gamma \lesssim 10$ ($t_{\rm obs} \gtrsim t_{\rm jet}$), $N_{\rm p}$ and $N_{\rm patch}$ share the same function (dashed line). Summarized information is given in Table 3.

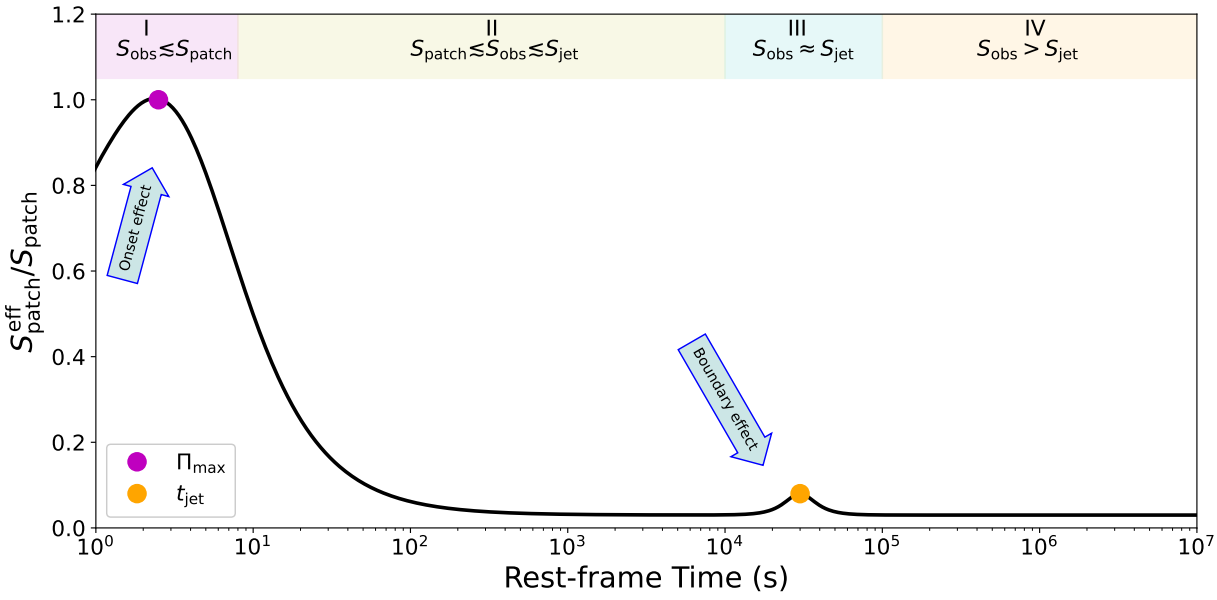

Figure 5: The solid line is qualitatively illustrated by the time evolution of $S^{\rm eff}_{\rm patch}/S_{\rm patch}$, while the data points with purple and orange colors indicate the $\Pi_{\rm max}$ point and the typical jet break time.

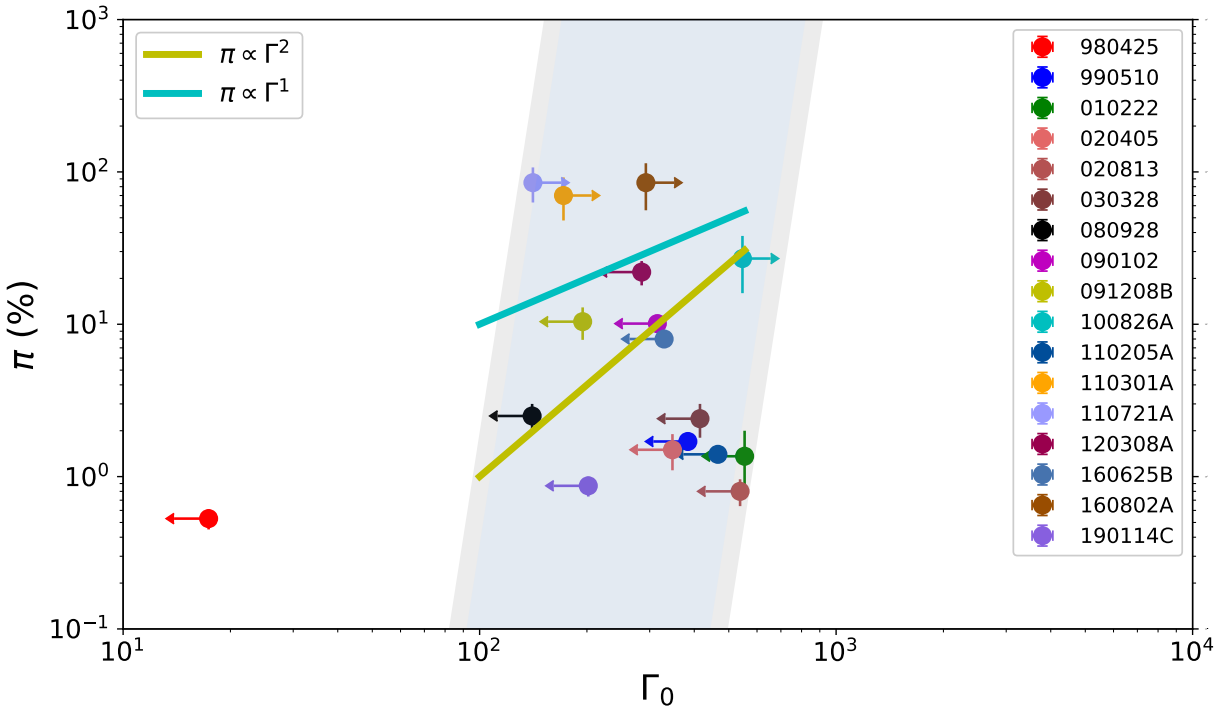

Figure 6: Time-integrated degrees of polarization $\pi_{\rm obs}$ as a function of the initial Lorentz factor Γ_0 at the deceleration radius, where Γ_0 is estimated by the empirical relation ($\Gamma_0 \simeq 249 L_{\gamma,{\rm iso},52}^{0.30}$). The cyan solid line represents the function of $\pi_{\rm obs} \propto \Gamma$ (Eq.22) for small polarization degree while the yellow solid line represents the function of $\pi_{\rm obs} \propto \Gamma^2$ (Eq.23) for large polarization degree. The rightward ($\Gamma_0 < \Gamma(\pi)$: prompt emission phase) and leftward ($\Gamma_0 > \Gamma(\pi)$: afterglow emission phase) arrows represent the region in which the bulk Lorentz factor is measured during the epoch of polarization.

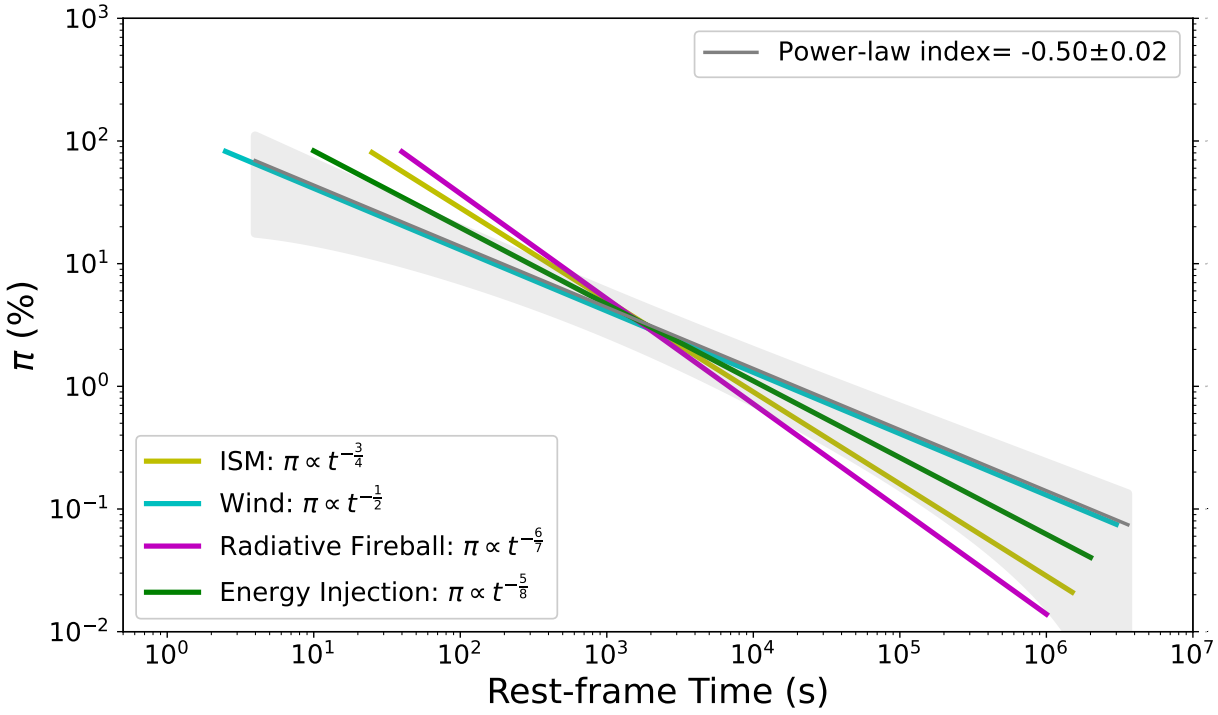

Figure 7: Comparing various afterglow models with observed results in the $\pi_{\rm obs}$-[t/(1+z)] plane. The solid line is the best fits using the power-law model from the observational data and with 2σ (95% confidence interval) error shadow region. The solid lines indicated by different colors represent different afterglow models.

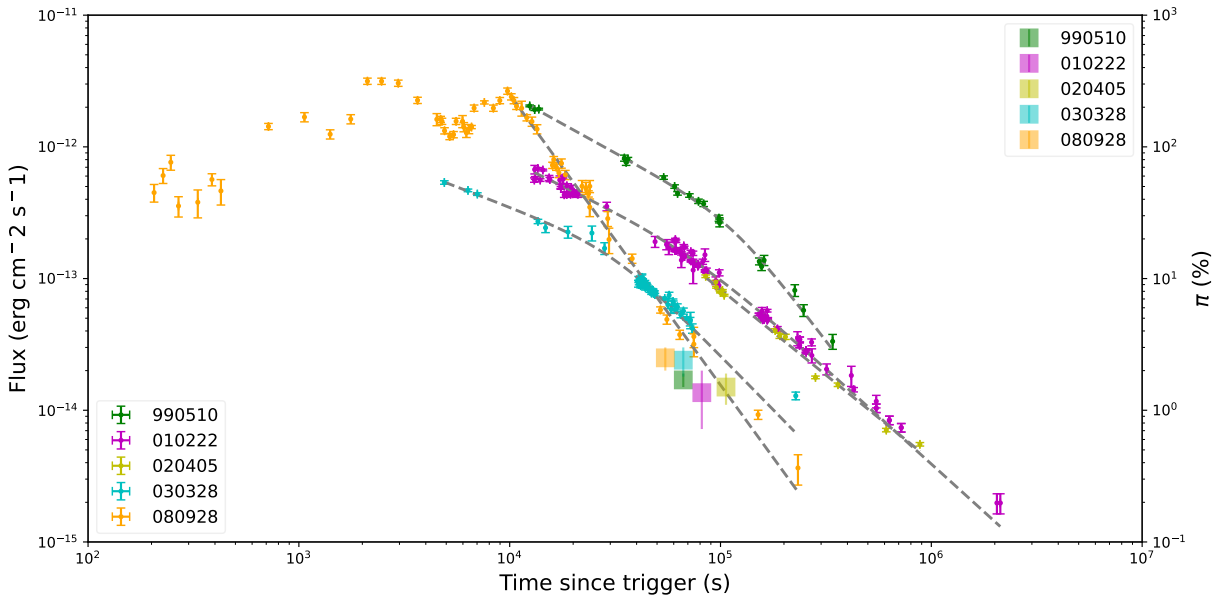

Figure 8: Optical (R-band) afterglow lightcurves (dotted lines) (left panel) and the degree of polarization (right panel) for the five bursts that have a jet break around the polarization epoch. (GRB 990510, GRB 010222, GRB 020405, GRB 030328, and GRB 080928). The dashed lines in left panel represent the best fits using a BKPL/SPL model.

Table 1 A full catalog of GRB polarimetric observations

GRB	PD ($\pi_{\rm obs}\%$)	PA ($^\circ$)	ν/keV	Energy/wave band	Time ($t-t_0$)	Significance	Instrument	Ref.	z
930131	>35	5	20 keV-1 MeV	γ-ray	NA	NA	BATSE-CGRO	[34]	NA
960924	>50	47	20 keV-1 MeV	γ-ray	NA	NA	BATSE-CGRO	[34]	NA
980329	<21	NA	8.3×10^9	Radio	500h	2σ	VLA	[35]	3.5ph[a]
980425	0.6	80	4000-7000 $\AA$	Optical	8days	NA	NA	[36]	0.0085
980425	0.4	67	4000-7000 $\AA$	Optical	25days	NA	NA	[36]	
980425	0.53±0.08	49±3	390-750 nm	Optical	42days	NA	CTIO 4-m telescope	[37]	
980703	<8	NA	4.86×10^9	Radio	100h	3σ	VLA	[1]	0.966
980703	<8	NA	8.46×10^9	Radio	100h	3σ	VLA	[1]	
990123	<2.3	NA	4.55×10^{14}	Optical(R)	18.25h	2σ	NOT	[38]	1.60
990123	$<23^l$,$<32^c$	NA	8.46×10^9	Radio	30h	3σ	VLA	[39]	
990510	1.7±0.2	101±3	4.55×10^{14}	Optical(R)	18.5h	NA	VLT	[2]	1.619
990510	1.6 ± 0.2	96±4	4.55×10^{14}	Optical(R)	20.6h	NA	VLT	[40]	
990510	<3.9	NA	4.55×10^{14}	Optical(R)	43h	NA	VLT	[40]	
990510	$2.2^{+1.1}_{-0.9}$	112^{+17}_{-15}	4.55×10^{14}	Optical(R)	43.4h	NA	VLT	[40]	
990712	2.9 ± 0.4	121.1±3.5	4.55×10^{14}	Optical(R)	10.56h	NA	VLT	[41]	0.434
990712	1.2 ± 0.4	116.2±10.1	4.55×10^{14}	Optical(R)	16.8h	NA	VLT	[41]	
990712	2.2 ± 0.7	139.1±10.4	4.55×10^{14}	Optical(R)	34.8h	NA	VLT	[41]	
991216	<2.7	NA	5.45×10^{14}	Optical(V)	35.0h	2σ	VLT	[42]	1.02?
991216	<5	NA	5.45×10^{14}	Optical(V)	60.0h	2σ	VLT	[42]	
991216	$<11^l$,$<17^c$	NA	8.46×10^9	Radio	35.8h	3σ	VLA	[12]	
991216	$<9^l$,$<15^c$	NA	8.46×10^9	Radio	64.3h	3σ	VLA	[12]	
000301C	<30	NA	4.55×10^{14}	Optical(R)	43.2h	NA	VLT	[43]	2.03
010222	1.36 ± 0.64	NA	5.45×10^{14}	Optical(V)	22.65h	NA	NOT	[44]	1.477
011211	<2.7	NA	4.55×10^{14}	Optical(R)	35h	3σ	VLT	[45]	2.14
020405	$<11^l$,$<19^c$	NA	8.46×10^9	Radio	28.6h	3σ	VLA	[12]	0.69
020405	1.50±0.40	172±8	4.55×10^{14}	Optical(R)	29.5h	NA	VLT	[46]	
020405	9.89±1.3	179.9±3.8	5.45×10^{14}	Optical(V)	31.7h	NA	MMT	[47]	
020405	1.96±0.33	154±5	5.45×10^{14}	Optical(V)	52.0h	NA	VLT	[48]	
020405	1.47±0.43	168±9	5.45×10^{14}	Optical(V)	76.2h	NA	VLT	[48]	
020813	1.8-2.4	153-162	$3.26\text{-}9.37\times10^{14}$	Optical	4.7-7.9h	NA	Keck	[49]	1.25
020813	0.80±0.16	144±6	NA	NA	13.92h	NA	NA	[50]	
020813	1.07±0.22	154.3±5.9	5.45×10^{14}	Optical(V)	21.55h	NA	VLT	[51]	
020813	1.42±0.25	137.0±4.4	5.45×10^{14}	Optical(V)	22.5h	NA	VLT	[51]	
020813	1.11±0.22	150.5±5.5	5.45×10^{14}	Optical(V)	23.41h	NA	VLT	[51]	
020813	1.05±0.23	146.4±6.2	5.45×10^{14}	Optical(V)	24.39h	NA	VLT	[51]	
020813	1.43±0.44	155.8±8.5	5.45×10^{14}	Optical(V)	26.80h	NA	VLT	[51]	
020813	1.07±0.53	163.0±14.6	5.45×10^{14}	Optical(V)	27.34h	NA	VLT	[51]	
020813	1.37±0.49	142.1±8.9	5.45×10^{14}	Optical(V)	27.78h	NA	VLT	[51]	
020813	1.26±0.34	164.7±7.4	5.45×10^{14}	Optical(V)	47.51h	NA	VLT	[51]	
020813	0.58±1.08	13.7±24.4	5.45×10^{14}	Optical(V)	97.29h	NA	VLT	[51]	
021004	1.88±0.46	189±7	4.55×10^{14}	Optical(R)	8.88h	NA	NOT	[52]	2.33
021004	2.24±0.51	175±6	4.55×10^{14}	Optical(R)	9.12h	NA	NOT	[52]	
021004	<0.60	NA	4.55×10^{14}	Optical(R)	9.60h	NA	NOT	[52]	
021004	0.71±0.13	140±5	5.45×10^{14}	Optical(V)	16.08h	NA	VLT	[52]	
021004	<5.0	NA	2.43×10^{14}	Optical(J)	10.76h	2σ	TNG	[53]	
021004	0.51±0.10	126±5	5.45×10^{14}	Optical(V)	14.62h	NA	VLT	[53]	
021004	0.8-1.7	100-147	$3.49\text{-}8.57\times10^{14}$	Optical	18.83h	NA	VLT	[53]	
021004	0.43±0.20	45±12	5.45×10^{14}	Optical(V)	90.7h	NA	VLT	[53]	
021206	80 ± 20	NA	150-2000 keV	γ-ray	NA	$\geq5.7\sigma$	RHESSI	[3]	NA
021206	0	NA	NA	NA	NA	NA	NA	[54]	
021206	<4.1	NA	150-2000 keV	γ-ray	NA	NA	NA	[54]	
021206	41^{+57}_{-44}	NA	150-2000 keV	γ-ray	NA	NA	RHESSI	[55]	
030226	<1.1	NA	4.55×10^{14}	Optical	25.39h	2σ	VLT	[56]	1.98
030328	2.4±0.6	170±7	5.45×10^{14}	Optical	18.5h	NA	VLT	[57]	1.52

GRB	PD ($\pi_{\rm obs}\%$)	PA ($^\circ$)	ν/keV	Energy band	Time ($t-t_0$)	Significance	Instrument	Ref.	z
030329	0.92±0.10	86.13±2.43	4.55×10^{14}	Optical(R)	12.77h	NA	VLT	[58]	0.168
030329	0.86±0.09	86.74±2.40	4.55×10^{14}	Optical(R)	13.18h	NA	VLT	[58]	
030329	0.87±0.09	88.60±2.64	4.55×10^{14}	Optical(R)	13.61h	NA	VLT	[58]	
030329	0.80±0.09	91.12±2.88	$3.53\text{-}4.55\times10^{14}$	Optical	14.04h	NA	VLT	[58]	
030329	0.66±0.07	78.52±2.94	4.55×10^{14}	Optical(R)	16.61h	NA	VLT	[58]	
030329	0.66±0.07	76.69±2.89	4.55×10^{14}	Optical(R)	17.11h	NA	VLT	[58]	
030329	0.56±0.05	74.37±3.11	4.55×10^{14}	Optical(R)	17.62h	NA	VLT	[58]	
030329	1.10±0.40	70±11	4.55×10^{14}	Optical(R)	36.72h	NA	CAHA	[58]	
030329	1.37±0.11	61.65±2.38	4.55×10^{14}	Optical(R)	37.20h	NA	VLT	[58]	
030329	1.50±0.12	62.29±2.44	4.55×10^{14}	Optical(R)	37.92h	NA	VLT	[58]	
030329	1.07±0.09	59.41±2.51	$3.53\text{-}4.55\times10^{14}$	Optical	40.08h	NA	VLT	[58]	
030329	1.09±0.08	66.07±2.45	4.55×10^{14}	Optical(R)	40.80h	NA	VLT	[58]	
030329	1.02±0.08	67.05±2.60	4.55×10^{14}	Optical(R)	41.28h	NA	VLT	[58]	
030329	1.13±0.08	70.56±2.51	4.55×10^{14}	Optical(R)	41.76h	NA	VLT	[58]	
030329	0.52±0.06	30.76±5.04	$3.53\text{-}4.55\times10^{14}$	Optical	64.32h	NA	VLT	[58]	
030329	0.52±0.12	12.55±4.63	4.55×10^{14}	Optical(R)	64.80h	NA	VLT	[58]	
030329	0.31±0.07	24.50±6.94	4.55×10^{14}	Optical(R)	65.28h	NA	VLT	[58]	
030329	0.57±0.09	52.85±4.08	4.55×10^{14}	Optical(R)	84.96h	NA	VLT	[58]	
030329	0.53±0.08	57.08±4.06	4.55×10^{14}	Optical(R)	85.44h	NA	VLT	[58]	
030329	0.42±0.10	62.21±6.10	4.55×10^{14}	Optical(R)	85.92h	NA	VLT	[58]	
030329	1.68±0.18	66.32±3.38	4.55×10^{14}	Optical(R)	135.84h	NA	NOT	[58]	
030329	2.22±0.28	75.16±3.32	4.55×10^{14}	Optical(R)	183.36h	NA	VLT	[58]	
030329	1.33±0.14	70.91±3.31	4.55×10^{14}	Optical(R)	230.16h	NA	VLT	[58]	
030329	2.04±0.57	1.16±7.64	4.55×10^{14}	Optical(R)	326.40h	NA	VLT	[58]	
030329	0.58±0.10	42.70±9.26	4.55×10^{14}	Optical(R)	540.00h	NA	VLT	[58]	
030329	1.49±0.56	99.71±6.60	4.55×10^{14}	Optical(R)	696.00h	NA	VLT	[58]	
030329	1.48±0.48	25.42±9.41	4.55×10^{14}	Optical(R)	900.00h	NA	VLT	[58]	
030329	2.10±1.20	54.1±10.4	4.55×10^{14}	Optical(R)	35.19h	NA	CAHA	[59]	
030329	1.97±0.48	83.2	4.55×10^{14}	Optical(R)	36.49h	NA	IAG-USP	[60]	
030329	<1	NA	8.4×10^{9}	Radio	185.04h	3σ	VLBA	[61]	
030329	<1.8	NA	8.4×10^{9}	Radio	1992h	3σ	VLBA	[62]	
030329	<4.7	NA	8.4×10^{9}	Radio	5208h	3σ	VLBA	[62]	
041219A	98±33	NA	100-350 keV	γ-ray	NA	$\sim2.3\sigma$	INTEGRAL-SPI	[63]	0.3
041219A	63^{+31}_{-30},96±40	70^{+14}_{-11}	100-350 keV	γ-ray	NA	$\sim2\sigma$	INTEGRAL-SPI	[64]	
041219A	≤ 4 and 43±25	38±16	200-800 keV	γ-ray	first and second peak	$<2\sigma$	INTEGRAL-IBIS	[65]	
060418	<8	NA	5.08×10^{14}	Optical	0.057h	2σ	LT	[4]	1.489
061122	29^{+25}_{-26},< 60	NA	100-1000 keV	γ-ray	NA	1σ	INTEGRAL-SPI	[66]	NA
061122	>33	160±20	250-800 keV	γ-ray	NA	90% confidence	INTEGRAL-IBIS	[67]	
071010	<1.3	NA	4.55×10^{14}	Optical	21.51h	3σ	VLT	[68]	0.98
080310	< 2.5	NA	5.45×10^{14}	Optical(V)	87171s	2σ	VLT	[69]	2.42
080310	< 2.5	NA	5.45×10^{14}	Optical(V)	169501s	2σ	VLT	[69]	
080310	< 2.6	NA	5.45×10^{14}	Optical(V)	253724s	2σ	VLT	[69]	
080928	2.5 ± 0.5	27±3	$4.25\text{-}6.00\times10^{14}$	Optical	15.2h	NA	VLT	[70]	1.692
090102	10.1 ± 1.3	NA	5.08×10^{14}	Optical	160.8-220.8s	$>3\sigma$	LT-RINGO	[71]	1.547
091018	<0.15[c]	NA	4.55×10^{14}	Optical(R)	3.74h	2σ	VLT	[72]	0.971
091018	<0.32	NA	4.55×10^{14}	Optical(R)	3.17h	1σ	VLT	[72]	
091018	0.21±0.31	177.0±47.5	4.55×10^{14}	Optical(R)	4.33h	NA	VLT	[72]	
091018	0.56±0.27	37.7±24.7	4.55×10^{14}	Optical(R)	4.73h	NA	VLT	[72]	
091018	0.26±0.31	9.2±43.7	4.55×10^{14}	Optical(R)	5.11h	NA	VLT	[72]	
091018	<0.32	NA	4.55×10^{14}	Optical(R)	5.53h	NA	VLT	[72]	
091018	1.07±0.30	179.2±16.1	4.55×10^{14}	Optical(R)	5.91h	NA	VLT	[72]	
091018	0.78±0.31	3.9±21.2	4.55×10^{14}	Optical(R)	6.33h	NA	VLT	[72]	
091018	0.84±0.30	171.1±19.9	4.55×10^{14}	Optical(R)	6.70h	NA	VLT	[72]	
091018	2.0±0.8	10.9±20.9	1.39×10^{14}	Optical(R)	10.34h	NA	VLT	[72]	
091018	1.44±0.32	2.2±12.6	4.55×10^{14}	Optical(R)	10.92h	NA	VLT	[72]	
091018	0.94±0.32	8.0±18.6	4.55×10^{14}	Optical(R)	11.30h	NA	VLT	[72]	
091018	1.73±0.36	69.8±11.7	4.55×10^{14}	Optical(R)	27.35h	NA	VLT	[72]	
091018	3.25±0.35	57.6±6.1	4.55×10^{14}	Optical(R)	27.73h	NA	VLT	[72]	
091018	1.99±0.35	27.6±10.0	4.55×10^{14}	Optical(R)	28.16h	NA	VLT	[72]	
091018	1.42±0.36	114.6±14.0	4.55×10^{14}	Optical(R)	28.54h	NA	VLT	[72]	
091018	0.27±0.38	101.6±47.1	4.55×10^{14}	Optical(R)	28.97h	NA	VLT	[72]	
091018	1.00±0.38	102.2±20.2	4.55×10^{14}	Optical(R)	29.35h	NA	VLT	[72]	
091018	0.41±0.34	168.8±36.6	4.55×10^{14}	Optical(R)	32.64h	NA	VLT	[72]	
091018	0.97±0.32	32.8±17.8	4.55×10^{14}	Optical(R)	33.40h	NA	VLT	[72]	
091018	1.08±0.35	88.7±17.9	4.55×10^{14}	Optical(R)	34.78h	NA	VLT	[72]	
091018	1.45±0.37	169.0±14.3	4.55×10^{14}	Optical(R)	55.37h	NA	VLT	[72]	
091208B	10.4 ± 2.5	92±6	4.55×10^{14}	Optical(R)	149-706s	NA	Kanata	[73]	1.063

Table 2: — continued

GRB	PD ($\pi_{\rm obs}\%$)	PA ($^\circ$)	ν/keV	Energy band	Time ($t-t_0$)	Significance	Instrument	Ref.	z
100826A	27 ± 11	159±18, 75±20	20 keV-10 MeV	γ-ray	0-100s	2.9σ	IKAROS-GAP	[74]	NA
100906A	<10	NA	$\sim 5\times10^{14}$	Optical	$\sim$0.5h	60%	MASTER	[75]	1.727
110205A	1.4	NA	4.55×10^{14}	Optical(R)	2.73-4.33hours	NA	CAHA	[76]	2.22
110205A	< 16	NA	5.08×10^{14}	Optical	243s	3σ	LT-RINGO2	[77]	
110205A	< 6.2	NA	5.08×10^{14}	Optical	0.93h	2σ	LT-RINGO2	[77]	
110301A	70 ± 22	73±11	10 keV-1 MeV	γ-ray	0-7s	3.7σ	IKAROS-GAP	[78]	NA
110721A	84^{+16}_{-28}	160±11	10 keV-1 MeV	γ-ray	0-11s	3.3σ	IKAROS-GAP	[78]	0.382
120308A	28 ± 4 to 16^{+5}_{-4}	34±4	5.08×10^{14}	Optical	$\sim$200-700s	3σ	LT-RINGO2	[22]	<4.5
120308A	23 ± 4	44±6	5.08×10^{14}	Optical	0.0594h	3σ	LT-RINGO2	[22]	
120308A	17^{+5}_{-4}	51±9	5.08×10^{14}	Optical	0.0892h	3σ	LT-RINGO2	[22]	
120308A	16^{+7}_{-4}	40±10	5.08×10^{14}	Optical	0.1189h	3σ	LT-RINGO2	[22]	
120308A	16^{+5}_{-4}	55±9	5.08×10^{14}	Optical	0.1792h	3σ	LT-RINGO2	[22]	
121011A	<15	NA	$\sim 5\times10^{14}$	Optical	$\sim$0.5h	60% confidence	MASTER	[79]	NA
121024A	0.61±0.13[c]	NA	4.55×10^{14}	Optical(R)	0.15days	NA	VLT	[80]	2.298
121024A	4.09±0.20	163.7±2.8	4.55×10^{14}	Optical(R)	2.69h	NA	VLT	[80]	
121024A	4.83±0.20	160.3±2.3	4.55×10^{14}	Optical(R)	2.96h	NA	VLT	[80]	
121024A	3.82±0.20	182.7±3.0	4.55×10^{14}	Optical(R)	4.11h	NA	VLT	[80]	
121024A	3.12±0.19	175.3±3.5	4.55×10^{14}	Optical(R)	4.46h	NA	VLT	[80]	
121024A	3.39±0.18	178.0±2.9	4.55×10^{14}	Optical(R)	4.84h	NA	VLT	[80]	
121024A	3.49±0.18	180.3±3.0	4.55×10^{14}	Optical(R)	5.23h	NA	VLT	[80]	
121024A	3.20±0.18	174.5±3.3	4.55×10^{14}	Optical(R)	5.62h	NA	VLT	[80]	
121024A	0.34±1.09	51.9±67.5	4.55×10^{14}	Optical(R)	23.45h	NA	VLT	[80]	
121024A	1.49±0.78	93.1±26.6	4.55×10^{14}	Optical(R)	26.62h	NA	VLT	[80]	
121024A	2.66±0.60	83.0±12.6	4.55×10^{14}	Optical(R)	28.62h	NA	VLT	[80]	
121024A	0.86±0.72	101.3±36.4	4.55×10^{14}	Optical(R)	29.39h	NA	VLT	[80]	
130427A	<3.9[l],<2.7[c]	NA	4.8×10^{9}	Radio	36h	3σ	EVN	[81]	0.3399
130427A	<7.5[l],<5.7[c]	NA	4.8×10^{9}	Radio	60h	3σ	EVN	[81]	
130427A	<21[l],<15[c]	NA	4.8×10^{9}	Radio	110h	3σ	EVN	[81]	
131030A	2.1 ± 1.6	27±22	4.55×10^{14}	Optical(R)	665s-2h	NA	Skinakas 1.3m	[82]	1.295
140206A	$> 28, > 48$?	80±15	15-350 keV	γ-ray	Second peak($\sim$4-26s)	90% confidence	INTEGRAL-IBIS	[83]	2.73
140430A	< 22	NA	5.08×10^{14}	Optical	124-424s	3σ	LT-RINGO3	[84]	NA
150301B	> 7.6	NA	5×10^{14}	Optical	79-89s	3.2σ	MASTER	[85]	1.5169
151006A	< 84	NA	100-300 keV	hard X-rays	NA	NA	*AstroSat*-CZTI	[7]	NA
160106A	68.5 ± 24	-22.5 ± 12	100-400 keV	hard X-rays	NA	$\gtrsim 3\sigma$	*AstroSat*-CZTI	[7]	NA
160131A	94 ± 31	41.2 ± 5	100-300 keV	hard X-rays	NA	$\gtrsim \mathbf{3}\sigma$	*AstroSat*-CZTI	[7]	0.972
160325A	58.75 ± 23.5	10.9 ± 17	100-300 keV	hard X-rays	NA	$\sim 2.2\sigma$	*AstroSat*-CZTI	[7]	NA
160509A	$< 92{,}96 \pm 40$	-28.6 ± 11	100-300 keV	hard X-rays	NA	$\sim 2.5\sigma$	*AstroSat*-CZTI	[7]	1.17
160530A	< 46	NA	0.2-5 MeV	soft γ-ray	NA	90% confidence	COSI	[86]	NA
160607A	< 77	NA	100-300 keV	hard X-rays	NA	NA	*AstroSat*-CZTI	[7]	NA
160623A	< 46	NA	100-300 keV	hard X-rays	NA	NA	*AstroSat*-CZTI	[7]	0.367
160625B	8.0±0.5	NA	NA	Optical	95-360s	$\mathbf{3}\sigma$	MASTER-IAC	[87]	1.406
160703A	< 55	NA	100-300 keV	hard X-rays	NA	NA	*AstroSat*-CZTI	[7]	<1.5ph
160802A	85±29	-36.1±4.6	200-300 keV	hard X-rays	NA	$\geq \mathbf{3}\sigma$	*AstroSat*-CZTI	[7]	NA
160802A	85±29	$\sim$-32	200-300 keV	hard X-rays	0-20.34s	$\sim \mathbf{3}\sigma$	*AstroSat*-CZTI	[88]	
160821A	48.7 ± 14.6	-34.0 ± 5.0	100-300 keV	hard X-rays	NA	$\geq \mathbf{3}\sigma$	*AstroSat*-CZTI	[7]	NA
160821A	21^{+24}_{-19}	NA	100-300 keV	hard X-rays	115-155s	2.2σ	*AstroSat*-CZTI	[89]	
160821A	66^{+26}_{-27}	NA	100-300 keV	hard X-rays	NA	$\sim 5.3\sigma$	*AstroSat*-CZTI	[89]	
160821A	71^{+29}_{-41}	110^{+14}_{-15}	100-300 keV	hard X-rays	115-129s	3.5σ	*AstroSat*-CZTI	[89]	
160821A	58^{+29}_{-30}	31^{+12}_{-10}	100-300 keV	hard X-rays	131-139s	4σ	*AstroSat*-CZTI	[89]	
160821A	61^{+39}_{-46}	110^{+25}_{-26}	100-300 keV	hard X-rays	142-155s	3.1σ	*AstroSat*-CZTI	[89]	
160821A	54 ± 21	-39±4	100-300 keV	hard X-rays	130-149s	$\geq 3\sigma$	*AstroSat*-CZTI	[90]	
160910A	93.7 ± 30.92	43.5 ± 4.0	100-300 keV	hard X-rays	NA	$\geq \mathbf{3}\sigma$	*AstroSat*-CZTI	[7]	NA
161203A	16^{+29}_{-15}	NA	50-500 keV	hard X-rays	NA	NA	POLAR	[90]	NA
161217C	21^{+30}_{-16}	NA	50-500 keV	hard X-rays	NA	NA	POLAR	[90]	NA
161218A	$7.0^{+10.7}_{-7.0}$	NA	50-500 keV	hard X-rays	NA	NA	POLAR	[90]	NA
161218A	<41%	NA	50-500 keV	hard X-rays	NA	99% confidence	POLAR	[6]	
161218B	13^{+28}_{-13}	NA	50-500 keV	hard X-rays	NA	NA	POLAR	[90]	NA
161229A	17^{+24}_{-13}	NA	50-500 keV	hard X-rays	NA	NA	POLAR	[90]	NA
170101A	$6.3^{+10.8}_{-6.3}$	NA	50-500 keV	hard X-rays	NA	NA	POLAR	[90]	NA
170101A	<30%	NA	50-500 keV	hard X-rays	NA	99% confidence	POLAR	[6]	
170101B	60^{+24}_{-36}	NA	50-500 keV	hard X-rays	NA	NA	POLAR	[90]	NA
170114A	$10.1^{+10.5}_{-7.4}$	NA	50-500 keV	hard X-rays	NA	NA	POLAR	[90]	NA
170114A	28±9[c]	NA	50-500 keV	hard X-rays	NA	NA	POLAR	[6]	
170114A	<28%	NA	50-500 keV	hard X-rays	NA	99% confidence	POLAR	[6]	

Table 2: — continued

GRB	PD ($\pi_{\rm obs}\%$)	PA ($^\circ$)	ν/keV	Energy band	Time ($t-t_0$)	Significance	Instrument	Ref.	z
170127C	$9.9^{+19.3}_{-8.4}$	NA	50-500 keV	hard X-rays	NA	NA	POLAR	[90]	NA
170127C	$<68\%$	NA	50-500 keV	hard X-rays	NA	99% confidence	POLAR	[6]	
170206A	$13.5^{+7.4}_{-8.6}$	NA	50-500 keV	hard X-rays	NA	NA	POLAR	[90]	NA
170206A	$<31\%$	NA	50-500 keV	hard X-rays	NA	99% confidence	POLAR	[6]	
170207A	$5.9^{+9.6}_{-5.9}$	NA	50-500 keV	hard X-rays	NA	NA	POLAR	[90]	NA
170210A	$11.4^{+35.7}_{-9.7}$	NA	50-500 keV	hard X-rays	NA	NA	POLAR	[90]	NA
170305A	40^{+25}_{-25}	NA	50-500 keV	hard X-rays	NA	NA	POLAR	[90]	NA
170320A	18^{+32}_{-18}	NA	50-500 keV	hard X-rays	NA	NA	POLAR	[90]	NA
170817A	<12	NA	2.8 GHz	Radio	244days	99% confidence	VLA	[91]	0.0093
171010A	$\sim$40	variable	100-300keV	hard X-rays	NA	NA	$AstroSat$-CZTI	[92]	0.3285
171205A	0.27±0.04	-71.3±3.3	97.5GHz	Radio	5.187 days	5σ	ALMA[1]	[93]	0.0368
171205A	0.30±0.06	-67.9±4.7	90.5GHz	Radio	5.187 days	5σ	ALMA	[93]	
171205A	$<$0.32	$<$-78.1	92.4GHz	Radio	5.187 days	5σ	ALMA	[93]	
171205A	0.35±0.08	-71.3±5.5	102.5GHz	Radio	5.187 days	5σ	ALMA	[93]	
171205A	0.31±0.06	-58.0±4.9	104.5GHz	Radio	5.187 days	5σ	ALMA	[93]	
190114C	0.87 ± 0.13	10±5	97.5×10^9	Radio	2.2-5.2h	$\geq5\sigma$	ALMA	[94]	0.425
190114C	0.60 ± 0.19	-44±12	97.5×10^9	Radio	2.2-5.2h	$\geq5\sigma$	ALMA	[94]	
190114C	7.7 ± 1.1 to 2-4	NA	NA	Optical	52-109s	NA	RINGO3	[95]	
190530A	55.43 ± 21.30	46.74±4.0	100-300keV	hard X-rays	0-25s	$\leq 3\sigma$	AstroSat-CZTI	[96]	0.9386
190530A	< 64.40	NA	100-300keV	hard X-rays	7.75-12.25s	95% confidence	AstroSat-CZTI	[96]	
190530A	53.95 ± 24.13	48.17±6.0	100-300keV	hard X-rays	12.25-25.0s	$\leq 3\sigma$	AstroSat-CZTI	[96]	
190530A	49.99 ± 21.80	49.61±6.0	100-300keV	hard X-rays	7.75-25.0s	$\leq 3\sigma$	AstroSat-CZTI	[96]	
190530A	< 65.29	NA	100-300keV	hard X-rays	15.0-19.5s	95% confidence	AstroSat-CZTI	[96]	
191016A	< 13.4	NA	V	Optical	3987-4587s	NA	LT-RINGO3	[97]	NA
191016A	5.7±5.6	82±26.4	V	Optical	4587-5187s	NA	LT-RINGO3	[97]	
191016A	< 10.8	NA	V	Optical	5187-5787s	NA	LT-RINGO3	[97]	
191016A	< 9.2	NA	V	Optical	5787-6387s	NA	LT-RINGO3	[97]	
191016A	< 13.5	NA	V	Optical	6387-6987s	NA	LT-RINGO3	[97]	
191016A	< 16.8	NA	V	Optical	6987-7587s	NA	LT-RINGO3	[97]	
191016A	< 9.1	NA	R	Optical	3987-4587s	NA	LT-RINGO3	[97]	
191016A	11.2±6.6	90.1±15.4	R	Optical	4587-5187s	NA	LT-RINGO3	[97]	
191016A	< 5.5	NA	R	Optical	5187-5787s	NA	LT-RINGO3	[97]	
191016A	6.1±6.0	89.8±30.5	R	Optical	5787-6387s	NA	LT-RINGO3	[97]	
191016A	< 12.0	NA	R	Optical	6387-6987s	NA	LT-RINGO3	[97]	
191016A	< 11.0	NA	R	Optical	6987-7587s	NA	LT-RINGO3	[97]	
191016A	4.7±4.1	93.16±22.6	I	Optical	3987-4587s	NA	LT-RINGO3	[97]	
191016A	< 5.2	NA	I	Optical	4587-5187s	NA	LT-RINGO3	[97]	
191016A	< 14.0	NA	I	Optical	5187-5787s	NA	LT-RINGO3	[97]	
191016A	14.6±7.2	100±12.4	I	Optical	5787-6387s	NA	LT-RINGO3	[97]	
191016A	< 10.7	NA	I	Optical	6387-6987s	NA	LT-RINGO3	[97]	
191016A	< 17.6	NA	I	Optical	6987-7587s	NA	LT-RINGO3	[97]	

The "Note".
(a): A photometric redshift is an estimate for the recession velocity of an astronomical object such as a galaxy or quasar, made without measuring its spectrum.
(l): Linear polarization measurements.
(c): Circular polarization measurements.
(1): The Atacama Large Millimeter/submillimeter Array.
(d): The Gamma-Ray Burst Polarimeter (GAP) on board the small solar-power-sail demonstrator IKAROS.
(e): The purpose-built RINGO2 polarimeter20 on the Liverpool Telescope.
(f): Compton Spectrometer and Imager.

Table 2: — continued

Extended Data Table 2 Polarimetric Observations in Different Segments

Segment	observed time $t_{\rm obs}$(s) (in the rest-frame)	observed area ($S_{\rm obs}$) (on the jet plane)	Γ	$\pi_{\rm obs}$	$\pi_{\rm obs}$(t)	$\pi_{\rm obs}(S_{\rm obs},\Gamma)$	$N_{\rm p}$	$N_{\rm patch}$ $(S_{\rm obs}/S_{\rm patch})$	$N_{\rm obs}$ $(S_{\rm jet}/S_{\rm patch})(S_{\rm jet}/S_{\rm obs})$
I	$\lesssim t_{\rm patch}(0\sim3)$	$\lesssim S_{\rm patch}$	>300	$\lesssim\Pi_{\rm max}$	increase	$\propto 1/S_{\rm obs},\propto\Gamma^2$	$\lesssim$1	$\approx$900	$>$900
$\Pi_{\rm max}$	$\approx t_{\rm patch}(\sim3)$	$\approx S_{\rm patch}$	≈300	$\approx\Pi_{\rm max}$	$\propto t^{-0.50\pm0.02}$	$\propto 1/S_{\rm obs},\propto\Gamma^2$	$\approx$ 1	$\approx$900	$\approx$900
II	$t_{\rm patch}\lesssim t_{\rm obs}\lesssim t_{\rm jet}\ (3\sim3\times10^4)$	$S_{\rm patch}\lesssim S_{\rm obs}\lesssim S_{\rm jet}$	≈50	$<\Pi_{\rm max}$	$\propto t^{-0.50\pm0.02}$	$\propto 1/S_{\rm obs},\propto\Gamma^2$	$>$1	$\approx$900	$\approx$25
III	$\approx t_{\rm jet}(10^4\sim10^5)$	$\approx S_{\rm jet}$	≈10	$<\Pi_{\rm max}$	increase	$\propto 1/S_{\rm obs},\propto\Gamma^2$	$\approx$900	$\approx$900	$\approx$1
IV	$>t_{\rm jet}(>10^5)$	$>S_{\rm jet}$	≈1	$<\Pi_{\rm max}$	$\propto t^{-0.21\pm0.08}$	$\propto 1/S_{\rm obs},\propto\Gamma^2$	$\approx$900	$\approx$900	$\approx$1

Extended Data Table 3 Fit Results for the Optical Afterglow Lightcurve (Jet Breaks)

GRB	$t_{\rm start}\sim t_{\rm stop}$ (10^4 s)	Model	α_1	$t_{\rm break}$ (10^4 s)	α_2	Is a jet break?
990510(R)	1.24∼34.02	BKPL	0.88±0.02	11.4 ± 1.3	2.11±0.30	Yes
010222(R)	1.31∼212.48	BKPL	0.67±0.15	12.3 ± 9.3	1.86±0.48	Likely
020405(R)	8.50∼88.26	SPL	...	...	1.30±0.05	No
030328(R)	0.49∼22.75	BKPL	0.54±0.06	4.81±0.89	2.20±0.31	Yes
080928($R_{\rm c}$)	0.02∼23.30	SPL	...	...	2.21±0.06 (Late part)	Yes

Extended Data Table 4 Results of Inferred Γ_0

GRB	$t_1 \sim t_2$ (s)	S	Detectors	$\Delta T_{\rm src}$ (s)	$[\Delta T_{\rm (bkg,1)}, \Delta T_{\rm (bkg,2)}]$ (s)	$F_\gamma^{\rm obs}$ (erg cm^{-2} s^{-1})	L_γ (erg s^{-1})	Γ_0
080928	-1∼14.336	11.67	(n3)n6n7b0	(-1 to 14.336)	(-20 to -10, 40 to 60)	$(6.13 \pm 3.98) \times 10^{-8}$	$(1.48 \pm 0.96) \times 10^{51}$	140
090102	-1∼26.624	44.69	n9na(nb)b1	(-1 to 26.624)	(-20 to -10, 180 to 200)	$(1.34 \pm 0.08) \times 10^{-6}$	$(2.19 \pm 0.13) \times 10^{52}$	315
091208B	-1∼12.480	32.93	n9(na)b0	(-1 to 12.48)	(-20 to -10, 40 to 60)	$(6.98 \pm 0.17) \times 10^{-7}$	$(4.39 \pm 1.07) \times 10^{51}$	195
100826A	-1∼82	11.67	n7(n8)b1	(-1 to 82)	(-20 to -10, 200 to 250)	$(3.92 \pm 0.25) \times 10^{-6}$	$(1.37 \pm 0.09) \times 10^{53}$	546
110301A	-1∼5.693	269.92	n7(n8)nbb1	(-1 to 5.693)	(-20 to -10, 40 to 60)	$(6.11 \pm 0.30) \times 10^{-6}$	$(2.96 \pm 0.14) \times 10^{51}$	173
110721A	-1∼21.822	84.67	(n6)n7n9b1	(-1 to 21.822)	(-20 to -10, 40 to 60)	$(3.76 \pm 0.40) \times 10^{-6}$	$(1.51 \pm 0.16) \times 10^{51}$	141
160625B	-1∼300	156.58	(n6)n7n9b1	(-1 to 300)	(-50 to -20, 80 to 100)	$(3.43 \pm 0.35) \times 10^{-6}$	$(2.54 \pm 0.26) \times 10^{52}$	329
160802A	-1∼20.34	151.65	(n2)b0	(-1 to 20.34)	(-20 to -10, 60 to 80)	$(4.87 \pm 0.49) \times 10^{-6}$	$(1.71 \pm 0.17) \times 10^{52}$	293
190114C	-1∼116.354	189.04	n3(n4)b0	(-1 to 116.354)	(-20 to -10, 180 to 200)	$(7.52 \pm 0.33) \times 10^{-6}$	$(4.96 \pm 0.22) \times 10^{51}$	202